Republic of Iraq
Ministry of Higher Education
and Scientific Research
University of Babylon
College of Education for Pure Science
Department of Physics

Nanolayers of Cu_2O Prepared by Thermal Evaporation Technique for optoelectronic Applications

A thesis
Submitted to the Council of the College of Education for Pure Sciences, University of Babylon in Partial Fulfillment of the Requirements for the Degree of Master in Education/ Physics

By
Ayat Abbas Obaid Kadim
B.Sc. in physics
(University of Babylon, 2017)

Supervised by

Prof. Khalid Haneen Abass, (Ph.D.)
College of Education for Pure Sciences
Department of Physics

2021 A.D. 1443A.H

بسم الله الرحمن الرحيم

(يَرْفَعِ اللَّهُ الَّذِينَ آمَنُوا مِنكُمْ
وَالَّذِينَ أُوتُوا الْعِلْمَ دَرَجَاتٍ)

صدق الله العلي العظيم

المجادلة ١١

Dedication

To Mesopotamia(Iraq) with honor and dignity...

To those, who lost their lives in a war without committing any crime...

To my first and dearest teacher my father...

To my mother whose love is planted in my heart...

To my brothers and sisters...,

To my close friends,

To my teachers who provided me with the keys of success

Ayat

Acknowledgement:

Allah, His Majesty, be praised for His incalculable bounties and best prayers, and peace be upon his best messenger Mohammed, his pure descendant, and his honorable companions. Then want to express my heartfelt gratitude and admiration for my instructors, Dr. Khaild Haneen Abass for his guidance, suggestions, and encouragement throughout the research work, without him, this thesis would have been impossible.

I would like to thank the staff of the department of Physics in College of Education for Pure Sciences in the University of Babylon for their kind attention and assistances.

Abstract

In this work, nanofilms were prepared from pure copper oxide (Cu_2O) with different thicknesses , t_1 , t_2 , t_3 , and t_4 in the range of 25,40,65,and 90 nm respectively .Thin films have been prepord by thermal evaporation technique under pressure of 1×10^{-7} mbar and the rate of deposition 0.5 nm/s on glass substrate at room temperature.

X-ray diffraction (XRD) results for Cu_2O films prepared on glass slides showed that the crystal system of the prepared films is cubic The surface topography was studied using atomic force microscopy (AFM). The measurements proved that the prepared films in this way have a homogeneous surface. Roughness average, root mean square and mean grain diameter increase with increasing of thickness. The scanning electron microscopy (SEM) image exhibited the grain diameter The grain diameter ranged between 8-20 nm. The average diameters of the nanoparticles were 11.65 nm, 9.03 nm 10.97 nm and 11.02 nm for t_1, t_2, t_3, and t_4 films respectively.

The results of the optical properties showed that the Cu_2O absorption rises with the thickness, while the transmittance decreases. Also, optical constants such as absorption coefficient, refractive index, extinction coefficient, real and imaginary dielectric constants, and dispersion parameters

Table of Contents

List of Tables

List of Figures

List of symbols and abbreviations

Symbols	Definition
μ	Mobility
A	Absorbance
a	Lattice Constant
C.B	Conduction Band
D	Average Grain Size
E_g	Energy Gap
ε_i	Imaginary Dielectric Constant
E_p	Energy of Absorbed
E_o	Single oscillator energy
ε_r	Real Dielectric Constant
hυ	Photon Energy
$k_\circ$	Extinction Coefficient
n	Refractive Index
n-type	Negative Electric Conductivity
p-type	Positive Electric Conductivity
PV	Photovoltaic solar cell

R.T	Room Temperature
Si	Silicon
T	Transmittance
t	Thickness
V.B	Valence Band
ZnO	Zinc Oxide
CuO	cupric oxide
eV	Electron Volt
α	Absorption Coefficient
λ	Wavelength
AFM	Atomic Force Microscopy
CVD	Chemical Vapor Deposition
emf	Electromotive Force
FWHM	Full Width at Half Maximum
UV	Ultra Violet Spectrum
ALE	Atomic Layer Epitaxy
XRD	X-Ray Diffraction
TF	Thin film
Cadet	cadmium telluride
CIGS	copper indium gallium dieseline
a-Si, TF-Si	amorphous and other thin-film silicon
ITO	indium tin oxide
PCE	power conversion efficiency
SCBD	seed layer-assisted chemical bath deposition
CW	continuous beam
PVD	physical vapor deposition
θ	Bragg angle
D	the inter-planar distant
β	the full width
E_g	energy gap
E_d	dispersion energy

1.1 Introduction

1.1.1 Thin Film Solar Cell

A thin film is a layer of material ranging from fractions of a nanometer (monolayer) to several micrometers in thickness, or second generation solar cell that is made by depositing one or more thin layers or thin film (TF) of photovoltaic material on a substrate, such as glass plastic or metal [1]. Film thickness varies from a few nanometers (nm) to tens of micrometers (μm), much thinner than thin-film's technology, the conventional. Thin film cells can be more flexible, lighter, and have less drag as a result of this [1]. In 1857, a scientist (Faraday) was able to create a thin metal film using a chemical reaction (Thermal Evaporation) [2].

The act of applying a thin film to a surface is thin-film deposition – any technique for depositing a thin film of material onto a substrate or onto previously deposited layers. "Thin" is a relative term, but most deposition techniques control layer thickness within a few tens of nanometers , Thin-film technologies are also being developed as a means of substantially reducing the cost of solar cells. The rationale for this is thin-film solar cells are cheaper to manufacture owing to their reduced material costs, energy costs [3]. Thin film technology is the basic of astounding development in solid state electronics, thin films are especially appropriate for applications in microelectronics [4].

Thin-film solar cells are commercially used in several technologies, including cadmium telluride (Cadet), copper indium gallium dieseline (CIGS), and amorphous and other thin-film silicon (a-Si, TF-Si) [5].

It's employed in integrated photovoltaic systems as well as semi-transparent photovoltaic glazing that may be laminated onto windows. In

some of the world's largest photovoltaic power facilities, stiff thin film solar panels (sandwiched between two panes of glass) are used in other commercial applications [6].

Other thin-film technologies are often classified as emerging or third generation photovoltaic cells and include; organic, dye-sensitized, and polymer solar cells, as well as quantum dot, copper zinc tin sulfide, nano crystal, micro morph and perovskite solar cells. Thin-film technologies reduce the amount of active material in a cell. It is possible to classify these techniques in two ways [7]: as shows at Fig. (1.1.)

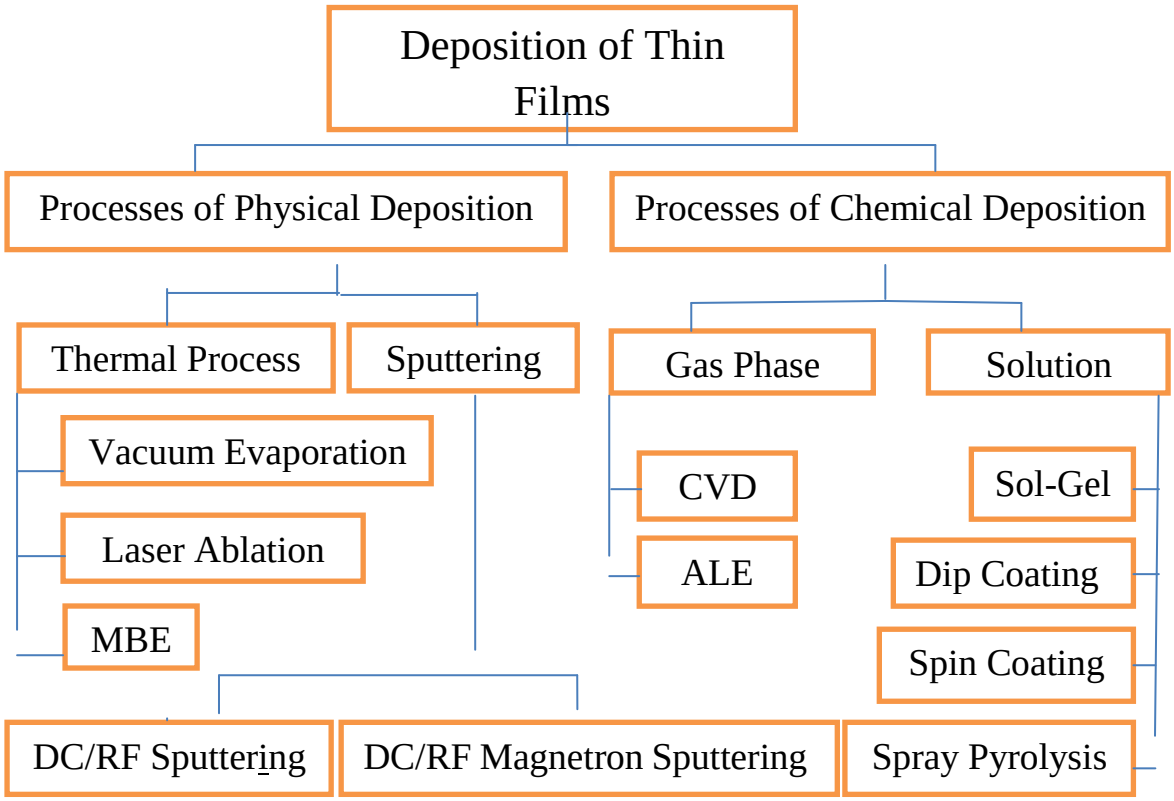

Fig. (1.1) Different physical and chemical thin film deposition processes [7].

1.1.2 Photovoltaic Solar Cell

The photovoltaic solar cell (PV) is considered a major element for obtaining energy from the sun because it can convert sunlight directly to electricity with high conversion efficiency. It can provide nearly permanent power at low operating cost, and is virtually free of pollution.

Recently, research and development have increased the low-cost flat-panel solar panels, thin-film devices, concentrator systems, and many innovative concepts [8].

The generation of voltage has been discovered by Becquerel in 1839 when a device is exposed to light, by a junction formed between an electrode and an electrolyte. The first photovoltaic effect of substantial (emf) voltage was noticed by Ohi on a silicon p-n junction in 1940 which is the main concern for solar cells and the power conversion efficiency [9].

Photovoltaic cells (PV) typically have at least two thin layers, one on top of the other, each with different dopants (deliberately inserted impurities). [10]. The result is that one layer is (n-type), with (negative) electrons added, and the other layer is (p-type), with positive holes added. As shown in Fig.(1.2), these two-layer structures are known as p-n junctions. resulting in an electric field (built-in) [11]. While photons form free electrons and holes around the p-n junction, the electric field in the area causes them to flow in opposite directions, the electrons to the n side and the holes to the p side. Between the p and n layers, an electric current (emf) is formed, with the p side positives and then half negative. When the p and n sides of a circuit are connected to a load, such as a light bulb or a calculator, a voltage is created and an electric current passes through the load. [12].

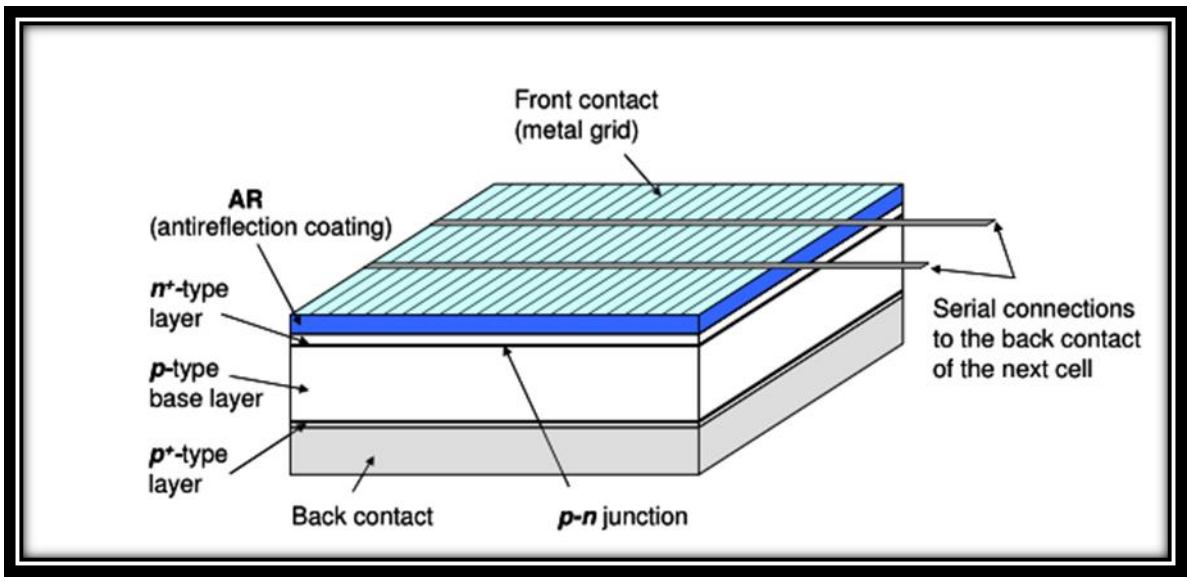

Fig. (1.2) Photovoltaic p-n junction solar cell [11]

1.2 Nanomaterials

Nanomaterials are materials with dimensions below 100 nm and they have at least one unique property that is different from the bulk material, or the study of material treatment on an atomic and molecular scale is the focus of science. Nanotechnology is the development of new processes and instruments with dimensions nanometers, which is a thousandth of a micrometer or a millionth of a millimeter. Nanotechnology deals primarily with atomic clusters spanning from five to one thousand atoms, with measurements ranging from 0.1 to 100 nm. [13].

The term "nano" is used as a prefix that denotes the ten base that is extended to the force of the (-9). The nanometer (denoted by nm) is the most accurate unit used to measure length, which is equal to 10^{-9} meters [14]. Nanotechnology is applied to various physical, chemical, biological, engineering, biomedical, medical and pharmaceutical sciences; it is used to design and manufacture tools and equipment in a scale not exceeding 100 nanometers by assembling the basic constituents of atoms. In

particular, the substitution of an atom of a seed element of another element produces different other substances. Sometimes, these substances surprise us with new characteristics that we did not know before; which opens up new areas for use and harnesses for the benefit of man [15-16].

Nanomaterials take several forms, each of which has a structure, characteristics, a measure of its diameter and length, and some of them also have distinct uses, and nanomaterials can be classified according to the form Fullerene, nanoballs, nanoparticles, Nanotubes, nanofibers, nanocomposites and Nanowires. nanomaterials are categorized according to their dimensions into four classes [17-18], which shown in Fig. (1.3)

1- Confinement in zero dimensions (quantum dots).
2- Confinement to a single dimension (quantum wires.).
3- Confinement in two dimensions (quantum wells).
4- Confinement in three dimensions (bulks).

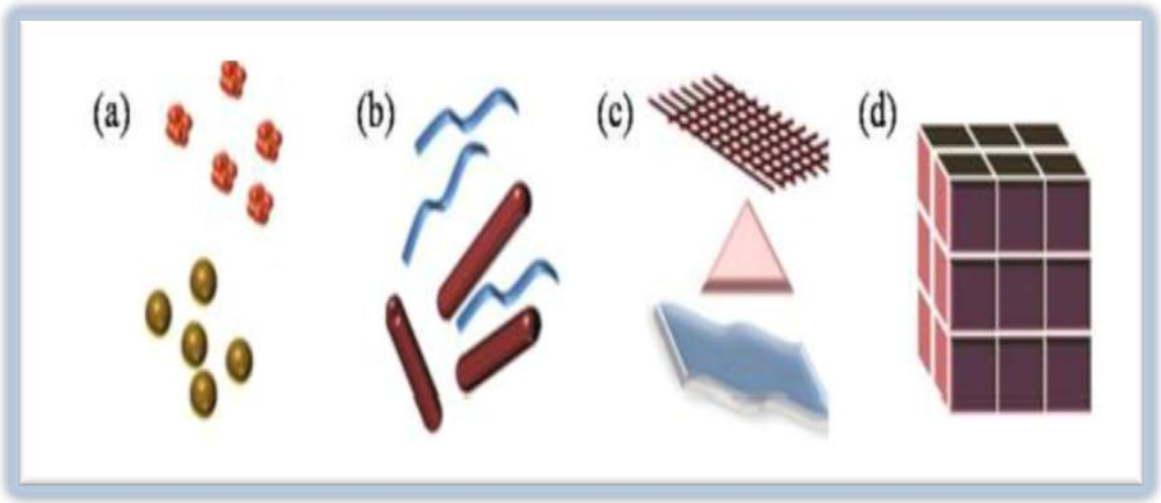

Fig. (1.3): Classification of Nanomaterials (a) 0D spheres and clusters, (b) 1D nanofibers, wires, and rods, (c) 2D films, plates, and networks, and (d) 3D nanomaterials [17-18].

1-3 Copper Oxide (Cu_2O)

Copper (I) oxide, also known as cuprous oxide, is one of the two main oxides of copper, the other being copper (II) oxide, also known as cupric oxide. CuO is a red-colored solid that is found in antifouling coatings. Copper (I) oxide is found as the reddish mineral cuprite and can look yellow or red depending on particle size [19]. It can be made in a variety of ways [20], the most straightforward of which is through the oxidation of copper metal:

$4Cu+O_2 \rightarrow 2Cu_2O$

Numerous properties such as non-toxic, earth-abundant, high optical transparency above 500 nm and high absorption coefficient [21]. It has a direct energy gap 2.17 eV, while the copper oxide is 1.7 eV [22].

1-3-1 The Cu_2O Properties

In terms of coordination spheres, the solid is diamagnetic, copper centers are 2-coordinated, and oxides are tetrahedral. In some ways, the concept is similar to the primary polymorphs of SiO_2, and both have formal or informal lattices. Copper (I) oxide combines in saturated ammonia solution to generate the colorless compound $[Cu(NH3)_2]^+$, which oxidizes to the blue $[Cu(NH3)_4\ (H2O)_2]^{2+}$ in air. Copper (II) sulfate and copper (II) nitrate are produced when it dissolves in hydrochloric acid, yielding $CuCl_2$ solutions. Dilute sulfuric acid and nitric acid generate copper (II) sulfate and copper (II) nitrate, accordingly. [23]

1.3.2. Properties of Semiconductors

Cu_2O is one of the most studied materials in semiconductor physics, and many experimental semiconductor applications have been shown initially in this material.
[24,26].

The lowest exactions in Cu_2O have a very long lifetime; absorption line geometries with negative line widths have been achieved, which is the smallest bulk exaction resonance ever observed. [27]. The associated quadruple Polaritons have a lower group velocity approaching sound speed. As a result, light in this medium moves nearly as slowly as sound, resulting in high polariton densities. Another unique aspect of ground state excitons is that all of their primary scattering mechanisms are quantifiable. [28]. Cu_2O was the first substance for which a completely parameter-free model of absorption line width broadening by temperature could be established, allowing the absorption coefficient to be calculated. The Kramers–Kronig relations do not apply to polaritons, as demonstrated by Cu_2O. [29].

1-3-3 Applications

Cuprous oxide is commonly used as a pigment, a fungicide, and an antifouling agent for marine paints. Rectifier diodes based on this material have been used industrially as early as 1924, long before silicon became the standard. Copper (I) oxide is also responsible for the pink color in a positive Benedict's test.[29]

1-4 Literature Survey

1- In 2011 Jeong, *et al.* [30] prepare carrier transport and recombination mechanisms in Cu_2O–ZnO heterojunction thin film solar cells and investigated through an analysis of their current–voltage characteristics in the dark and under various illumination intensities, as a function of temperature between 100 K and 295 K. The Cu_2O–ZnO heterojunction solar cells were prepared by metal organic chemical vapor deposition of Cu_2O on ZnO films sputtered on transparent conducting oxide coated glass substrates.

2- In 2012 Kidowaki, *et al.* [31] They use a spin-coating process to construct cuprous oxide (CuO)-based solar cells containing fullerene (C60) on indium tin oxide (ITO). Solar cells with the CuO/C60 construction have their microstructure and cell performance examined. Fabricate a photovoltaic device using an ITO/CuO/C60 hererojunction structure. X-ray diffraction was used to analyze the crystal structure of the CuO active layer. The current energy rates of solar cells are also reviewed.

3- In 2012 Gershon, *et al*. [32], a novel approach to overcoming the limitations of low long-wavelength absorption short charge transport lengths in electrodeposited bilayer ZnO/Cu_2O solar cells. They reduce the Cu_2O thickness to approximately the minority carrier transport length and coat a film of a semiconducting polymer between the Cu_2O and a top electrode

4- In 2012 Paracchino, *et al.* [33], a thorough investigation of the influence of electrode position settings on Cu_2O' photo-electrochemical properties. For this semiconductor, the effect of deposition variables (temperature, pH, and deposition current density) on conductivity has been extensively studied in the past. They

examine the photo activity of Cu_2O films deposited under various conditions and correlate the photo response to morphological features, film orientation, and electrochemical characteristics. Under chopped simulated AM 1.5 light, the photo-electrochemical response was studied using linear sweep voltammetry. For a film thickness of 1.3 m, the greatest photocurrent obtained was 2.4 mA cm^{-2} at 0.25 V versus RHE.

5- In 2013 Noda, *et al.* [34] they fabricate Cu_2O/ZnO heterojucntion solar cells were successfully obtained by a magnetrons putter deposition method. The Cu_2O thin film was deposited by the method using a sintered Cu_2O ceramics target. Crystalline phases of the films were controlled by adjusting an O_2 flow rate ratio (O_2/(Ar+O_2)) precisely during the sputtering process and Cu_2O single phase polycrystalline films were obtained at room temperature.

6- In 2015 Yu, *et al.* [35] they produce F-doped Cu_2O thin films with various F contents on ITO glass using a simple electrochemical deposition process. The produced F-doped Cu_2O thin films have n-type semiconductor properties and exhibit very high electrical and optical properties, particularly for the one with an F/Cu = 1:2 preparation molar ratio. This sample has a one-of-a-kind net microstructure that allows for the best visible light absorption, and its electron concentration is more than ten times higher than pure Cu_2O.

7- In 2016 Sboui., *et al.* [36] Hybrid paper–TiO_2, paper–Cu_2O–TiO_2, and paper–TiO_2–Cu_2O photo catalysts were made using a nonhydrolytic sol–gel procedure, moderate hydrothermal treatment to manufacture the TiO_2 layer, and a reduction method to make the Cu_2O nanoparticles. Raman, TGA, FE-SEM, UV-Vis, and XPS were used to characterize the hybrid photo catalysts. The immobilized TiO_2 was discovered to generate a homogenous thin layer of nanoparticles

smaller than 10 nm in size. Cu_2O nanoparticles with diameters ranging from 30 to 100 nm were created on top of the TiO_2 layer or by reducing Cu_2+ ions. When subjected to simulant solar light, all of the produced hybrid catalysts demonstrated effective photo catalytic capabilities for the degradation of toluidine.

8- In 2018 Zang [37] Because of its low cost, nontoxicity, and high mobility, Cu_2O is one of the most appealing photovoltaic materials for solar cells. With properly aligned and micrometer grain sized Cu_2O films, an obvious increase in power conversion efficiency (PCE) for ZnO/Cu_2O solar cells was proven experimentally. Cu_2O was made by oxidizing Cu foils with a radical at a low temperature of 500°C. Perfectly aligned and micrometer sized Cu_2O crystals (3 4 lm) could be formed after a quick quenching and post annealing treatment. Cu_2O's crystal structure and optical characteristics were studied in depth. The PCE of solar cells based on Cu_2O with treatment was 3.18 percent, leading to a considerable PCE improvement of 60.6 percent when compared to conventional solar cells without any treatment.

9- In 2018 Khan, *et al.* [38] they are getting ready Thermal evaporators deposit polycrystalline cuprous oxide (p-Cu_2O) films on Cu substrates for various oxygen pressures (OP) (0.2, 0.3, and 0.4 mbar).. The Cu (200), Cu_2O (200), and Cu_2O (200) XRD patterns demonstrate the evolution of Cu (200), Cu_2O (200), and Cu_2O (200). (311) The spacing and lattice constant, respectively, are 0.210, 0.128 nm and 0.421, 0.425 nm.. With increasing OP, the thickness and growth rate of P-Cu_2O films are determined to be 87.9, 71.9, 65.5 nm and 17.6, 14.2, 13.1 (nm min-1).

10- In 2020 Tuama, *et al.* [39], they prepare Cupreous oxide (Cu_2O) nanofilms by thermal evaporation technique with various thickness (50, 65, 75 nm). Surface morphological properties of Cu_2O films were

examined via atomic force microscope (AFM). The root mean square, average roughness, number of grains on surface, and average diameter are studied from atomic force microscopy. The optical properties were studied from recording the absorption spectra via UV-Visible spectrophotometer in the wavelength range of 190-1100 nm.

11- In 2020 Kara, *et al.* [40] they used a simple two-step electro-deposition procedure to successfully manufacture Cu2O: Na/ZnO/FTO heterojunctions. The effects of Na doping on the electronic, morphological, microstructural, optical, and electrical properties of nanostructures were studied. The deposition took place at different Na ion concentrations and a constant bath temperature (70 °C). The selective potential for electrode position of pure Cu_2O was determined using cyclic voltammetry. The Cu_2O layers had p-type conductivity, while the ZnO films had n-type conductivity, according to Mott-Schottky electrochemical impedance study. All doped and undoped Cu_2O nanostructures have a polycrystalline nature, according to X-ray diffraction investigation, with highly cubic Cu_2O (111) oriented crystallites and a hexagonal wurtzite structure of ZnO with (002) sample treated.

12- In 2021 Kumar, *et al.* [41] We used the sol–gel process to make CuO and Cu_2O nanoparticles for use in photovoltaic and energy storage systems.. The production of pure CuO and Cu_2O nanostructures with average crystallite sizes of 31.9 and 39.3 nm, respectively, is clearly seen in the XRD pattern. The creation of pure CuO and Cu_2O nanoparticles is also confirmed by FTIR spectroscopy. CuO and Cu_2O have optical energy band gaps of 2.18 eV and 1.62 eV, respectively, as predicted from tauc's figure. The photoluminescence spectra's broad and visible emission peaks are linked to the

superposition of numerous flaws in the matching CuO and Cu_2O nanostructures.

13- In 2021 Alsultany. *et al*. [42] manufacture homogeneous and excellent crystal quality cuprous oxide (Cu2O) nanoparticles on transparent conductive/glass substrates, a seed layer-assisted chemical bath deposition (SCBD) approach at low temperature has been devised. Prior to producing the Cu_2O nanoparticles, the ITO seed annealing procedure was performed with a continuous beam (CW) CO_2 laser.. Controlled synthesis of Cu_2O lms was explored in this study by adjusting the growth temperature to 55, 60, 65, and 70 degrees Celsius, respectively. The work proposes a synth20etic strategy for generating high-quality Cu_2O nanoparticles for optical and electrical applications utilizing the SCBD approach.

1-5 Aim of the Work

In this study, thermal evaporation technique was used to fabricate nano-layers with very fine particle size from Cu_2O nanoparticles. Nano-layers were formed for low refractive index, and study the structure and optical properties to candidate these films for optical devices.

2.1 Introduction

This chapter focuses on the theoretical part, which represent by thermal evaporation: optimization, advantages, disadvantages, specifications of the system as well as structural and morphological properties (X-ray diffraction, atomic force microscopy (AFM) and scanning electron microscope (SEM)), optical properties of crystalline semiconductors (the electronic transitions, optical constants, and dispersion parameters).

2.2 Thermal Evaporation

An electric resistance heater melts the material and raises the vapor pressure to a practical range in a thermal evaporator. This is done at a high vacuum to prevent the vapor from interacting with or scattering against other gas-phase atoms in the chamber, as well as to reduce the incorporation of contaminants from the residual gas in the vacuum chamber. [43.44]. Thermal evaporation is the most straightforward method of depositing material onto a substrate at a pressure of 1×10^{-7} mbar, with high film quality. The configuration of a basic coating system is shown in Figure (2.1) [45, 46].

A thermal evaporation is a common method of physical vapor deposition (PVD). It is one of the simplest forms of PVD and typically uses a resistive heat source to evaporate a solid material in a vacuum environment form a thin film.

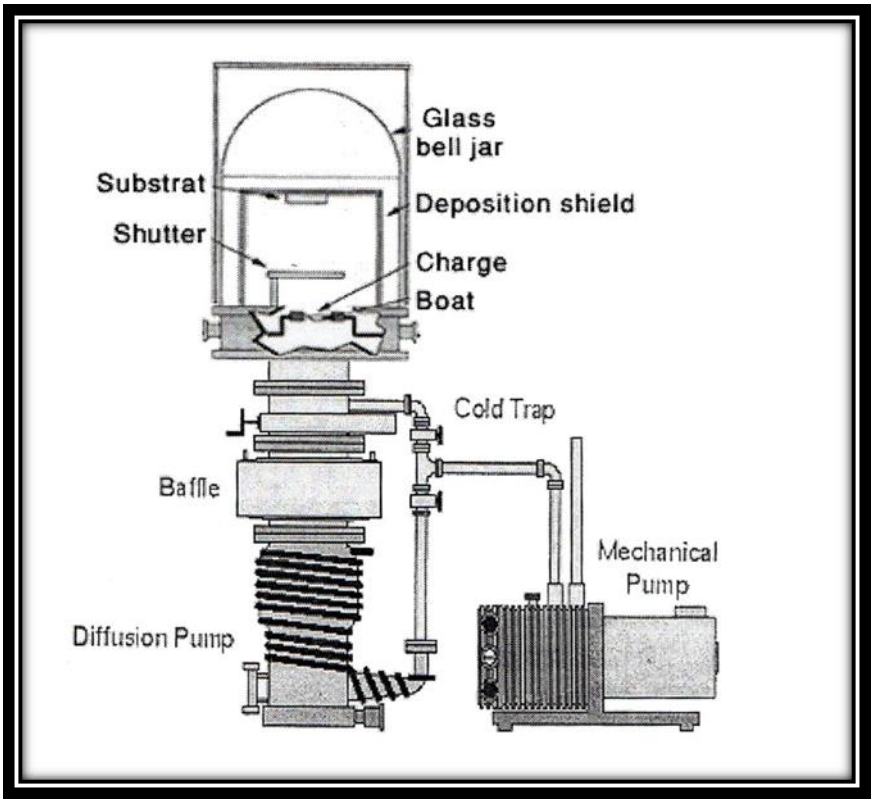

Fig. (2.1): Configuration of a basic coating system [45, 46].

2.3 Structural and Morphological Properties:

2.3.1 X-ray diffraction (XRD)

X-ray diffraction (XRD) is a technique for determining the atomic structure of materials at the atomic level. The method is based on the fact that X-ray wavelengths are the same size as the distances between atoms in condensed materials. When a material exhibits a long-range (at least m-range) periodic atomic order, this is referred to as a periodic atomic order., It is bombarded with X-rays and behaves as an extended periodic grating, producing a diffraction pattern with several sharp spots known as Bragg diffraction peaks. [47]. The spatial features of the grating can be determined by measuring and evaluating the positions and intensities of the Bragg peaks. The three-dimensional (3D) atomic arrangement in crystalline materials must be determined. This is the essence of XRD so-called "crystal structure" analysis. [47]. When a monochromatic X-ray beam strikes a crystal sample, constructive diffractions (or interference)

from parallel planes of atoms with inter-planar spacing (d) occur, as seen in Fig (2.2) if Bragg's law holds true [48].

$$2d\sin\theta = n\lambda \qquad (2\text{-}1)$$

where n is integer that shows the order of the reflection, θ is Bragg angle, and λ is the wavelength of the x-ray beam, (d) the inter-planar distant.

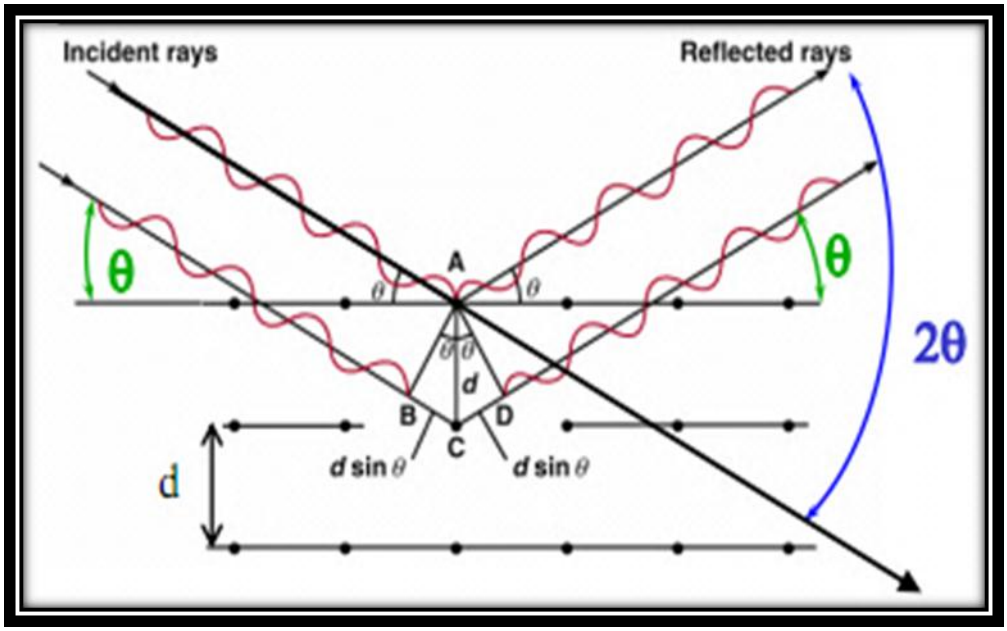

Fig. (2.2): Bragg diffraction [48].

2.3.1.1 Parameters' Calculation

Normally XRD is used to calculate different parameters, which could be used to clarify the studies of the deposited films.

1. Full width at half maximum (FWHM) (β)

Full width at the half of the maximum intensity (FWHM). The FWHM of the preferred orientation (peak) could be measured, since it is equal to the width of the line profile (in degrees) at the half of the maximum intensity [49].

2. Average crystallite size (D)

The crystallite size (D), can be estimated using the Scherer's formula [50] :

$$D = 0.9\lambda / \beta \cos\theta \qquad (2\text{-}2)$$

where λ is the X-ray wavelength (Å) , β is the full width at the half of the maximum intensity (FWHM) (radian), θ is Bragg diffraction angle of the XRD peak (degree).

2.3.2 Scanning Electron Microscopy (SEM)

Scanning electron microscopy (SEM) is an important tool to investigate the surface and morphology of nanostructures. We may use it to calculate the nanostructures' diameter, length, thickness, density, form, and orientation. The schematic diagram of the SEM apparatus is shown in Fig (2.3). [51]. Warming an electron gun made of tungsten filament emits electrons, which are then guided and focused on the specimen by an anode and various electromagnetic lenses placed between both the electron gun and the specimen. After striking the sample, these projected electrons emit secondary and back scattered electrons. Indexer the secondary and back scattered electrons expelled from the sample, and these detectors convert the discovered electrons into an electronic signal that is supplied to a computer.[51]

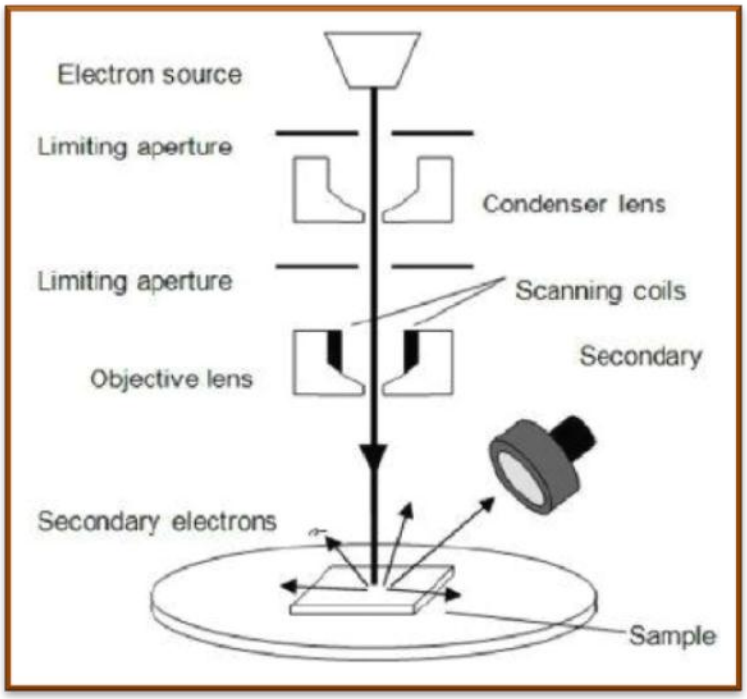

Fig. (2.3): Schematic diagram of the scanning electron microscopy [52].

2.3.3 Atomic Force Microscopy (AFM)

AFM (atomic force microscope) is a sort of scanning probe microscopy with a resolution of fractions of a nanometer, which is more than 1000 times higher than the optical absorption edge. In 1986, Binnig, Quite, and Gerber developed the first AFM. One of the most important technologies for photographing, measuring, and manipulating materials at the nanoscale is the AFM. The word "microscope" in the title is a misnomer because it indicates that the information is collected by "feeling" the surface with a mechanical probe, rather than by looking at it. Piezoelectric components offer very fine scanning by allowing tiny but accurate and exact movements on (electronic) command. [53].

The block diagram of AFM is shown in Figure (2.4). The AFM is made up of a microscale cantilever with a sharp tip (probe) that is used to scan the surface of the material The AFM scans a surface using a fine ceramic or semiconductor tip, similar to how a phonograph needle scans a record. When the tip comes into contact with a sample surface [53], Van

der Waals forces between the tip and the sample cause the cantilever to deflect. A laser reflects at an oblique angle from the very end of the cantilever, capturing the magnitude of the deflection. The resolution of the hills and valleys that make up the surface topography can be determined by plotting laser deflection versus tip position on the sample surface [54]. The tip of the AFM can either touch the sample (contact mode) or tap across the surface (tapping mode), similar to a blind person's cane. [55].

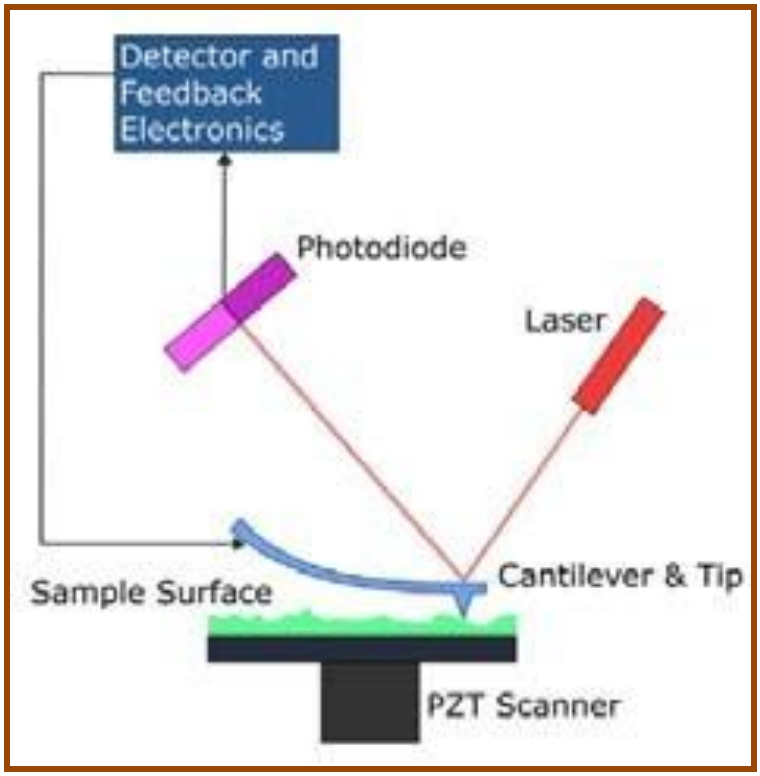

Fig. (2.4): Block diagram of atomic force microscope [54].

2.4. Optical Characters of Crystalline Semiconductors

When a photon's energy ($h\upsilon$) is equal to or greater than the forbidden energy gap (E_g) in crystalline semiconductors, an electron in the valence band absorbs high energy from the incident photon in order to escape to the conduction band. [56].

$$h\upsilon \geq E_g \qquad (2\text{-}3)$$

where (υ) is the frequency in Hertz (Hz), and (h) is the Plank constant (6.62510^{-34}J.s), and The spectroscopy of the incident rays region that initiates electron transport is known as (fundamental absorption edge). The basic absorption edge is one of the most noticeable aspects of a semiconductor's absorption spectrum.It equals the difference between the top valence band and the bottom conduction band.as shiw in Fig. (2.5) [57].

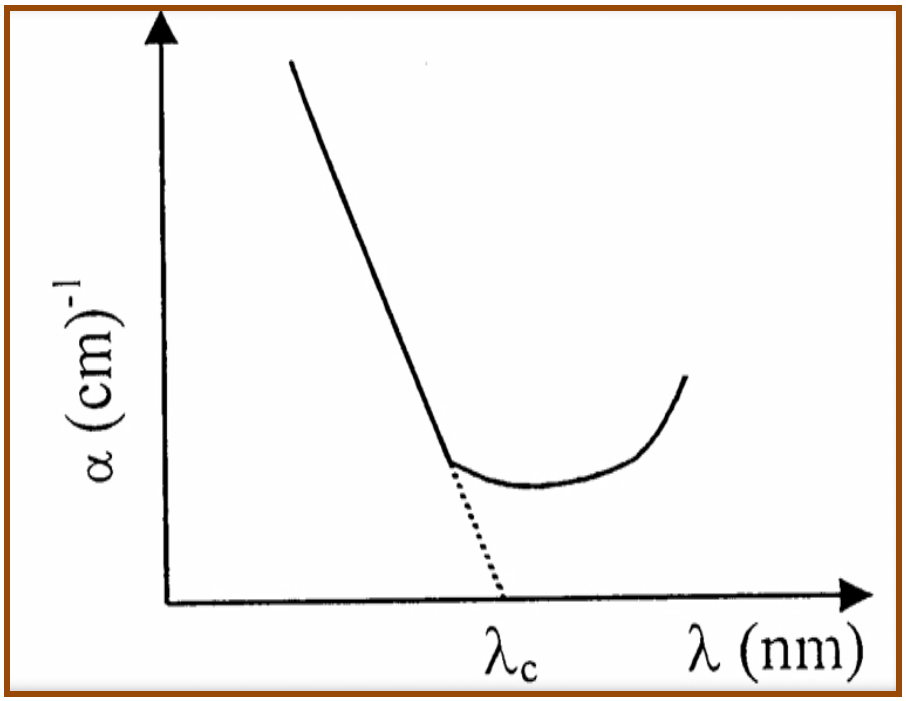

Fig (2.5) Crystalline semiconductor fundamental absorption edge [57].

When (E_g=hυ◦), where (ν_o) is called critical frequency and the wavelength facing it is called wavelength cut off (λ_c). This process happens when the width of forbidden energy gap equals to incident energy photon which can be expressed in equation (2.3) [58],

$\lambda = hc / E_g = 1.24 / E_g$ (2-4)

where (c) is speed of light in vacuum

2.4.1 .The Electronics Transition:

The electrical transitions can be divided into two categories [59]:

2.4.1.1. Directly transitions:

When the bottom of the conduction band (C.B) is exactly over the top of the valence band in semiconductors, this transition occurs (V.B). This indicates that their wave vectors have the same value (K=0). When (E_g=hυ), the absorption appears in this state. The rules of conservation of energy and momentum were required for this transition type. Direct transitions are divided into two categories: [60],

a- **Allowed direct transition**

Fig (2.6.a) shows these transitions occur between the top and bottom points of the (V.B) and (C.B). The equation gives the empirical relationship for this type of transition. [60],

$\alpha h\upsilon \approx [h\upsilon - E_g]^{1\backslash 2}$ (2-5)

Where (α) is the absorption coefficient

b- Forbidden direct transitions

Figure (2.6.b) shows these transitions take place between the top and bottom points of (V.B) and (C.B). The equation represents the empirical relationship that corresponds to this transition. [61],

$\alpha h\upsilon \approx [h\upsilon - E_g]^{3\backslash 2}$ (2-6)

2.4.1.2 Indirect Transitions

This transition happens when In curve, the bottom of (C.B) is not over the top of (V.B) (E-K). The electron transits from (V.B) in a non-perpendicular manner, with the wave vector of the electron before and after the transition not equal ($\Delta K \neq 0$). For the conservation of energy and momentum law, this transition type occurs with the help of a similar particle named "Phonon." As a result, the assistance of a phonon is required to con [61],

$$h\upsilon = E_g \pm E_p \quad (2\text{-}7)$$

$$hk_f = hk_i \pm hk_p \quad (2\text{-}8)$$

where E_p is the energy of absorbed or emitted phonon.

1- **Allowed indirect transitions**

Fig (2.6.c) shows these transition occuring between the top of (V.B) and the bottom of (C.B) which are found in the difference region of (K-space), so that [61],

$$\alpha h\upsilon \approx [h\upsilon - E_g]^2 \quad (2\text{-}9)$$

2- **Forbidden indirect transitions**

Fig (2.6.d) shows these transitions occurring between near points in the top of V.B and near points in the bottom of C.B. The absorption coefficient for transition with a phonon absorption is given by the following equation [62],

$$\alpha h\upsilon \approx [h\upsilon - E_g]^3 \quad (2\text{-}10)$$

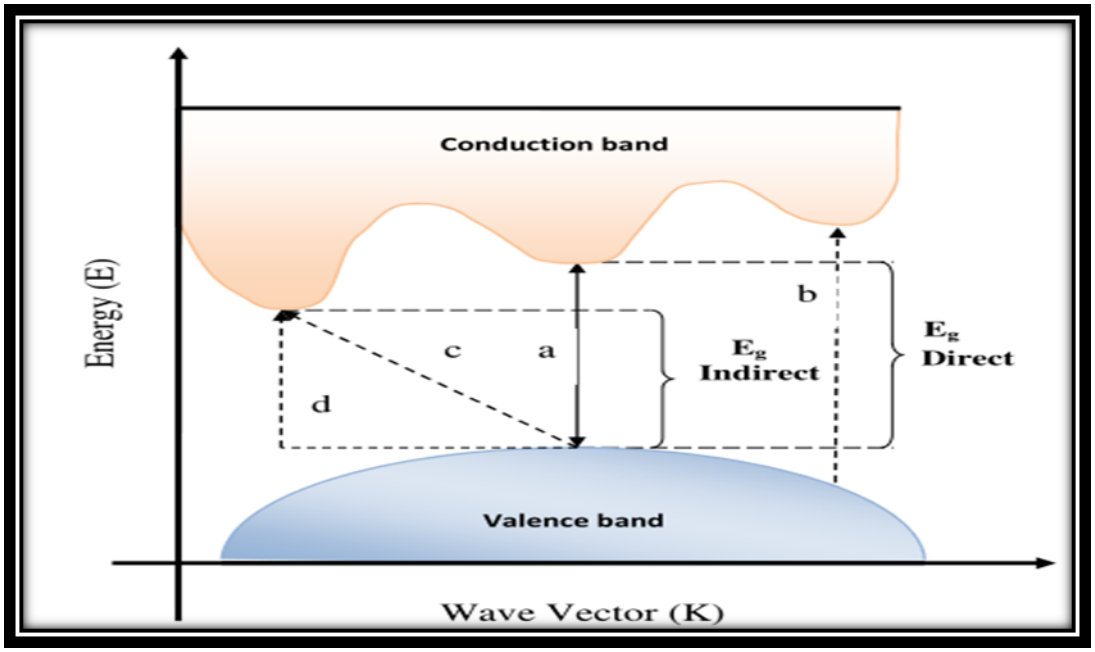

Fig. (2.6): The types of transition [60]:
(a) allowed direct, (b) forbidden direct, (c) allowed indirect, (d) forbidden indirect.

2.4.2 Optical Constant:

Because they characterize the optical behavior of materials, optical constants are particularly important parameters. The extraction of optical constants from various forms of optical measurements is a popular topic of study. [63]. The refractive index (n), extinction coefficient (k_0), and real (_r) and imaginary I components of the dielectric constant were among the optical constants. The refractive index is a quantity that is connected to reflectance and is defined as [64]:

$$n = \left[\frac{4R}{(R-1)^2} - k_\circ{}^2\right]^{\frac{1}{2}} + \frac{(R+1)}{(R-1)} \quad (2-11)$$

where (R) is the reflectance.

The extinction coefficient ($k_\circ$) is related to the exponential decay of the wave as it passes through the medium and it is defined as [65]:

$$k_\circ = \frac{\alpha\lambda}{4\pi} \quad (2.12)$$

where (α) is given by [65]:

$$\alpha = 2.303\frac{A}{t} \quad (2.13)$$

The absorbance is (A) and the sample thickness is (t). And (R) is derived from the equation below. [65]:

$$R + T + A = 1 \quad (2.14)$$

Dielectric constant represents the ability of material to polarization, whose expression, is given by the following equation [66]:

$$\varepsilon = \varepsilon_r - i\varepsilon_i \quad (2.15)$$

$$\varepsilon = (n)^2 \quad (2.16)$$

$$(n - ik_\circ)^2 = \varepsilon_r - i\varepsilon_i \quad (2.17)$$

$$\varepsilon = \left(n^2 - k_\circ{}^2\right) - i(2nk_\circ) \quad (2.18)$$

From equations (2.17) and (2.18), real and imaginary represent function of complex dielectric coefficient which can be written as in following equation [66],

$$\varepsilon_r = n^2 - k_\circ^{\,2} \quad (2.19)$$

$$\varepsilon_i = 2nk_\circ \quad (2.20)$$

2-5 Dispersion parameters

They introduced an energy parameter, E_d , to describe the dispersion of the refractive index. In terms of this dispersion energy, E_d , and single oscillator energy, E_o , the refractive index can be expressed in the form (2-21) and (2-22).

$$n^2 - 1 = E_d E_o \backslash E^2_o - (hv)^2 \quad (2\text{-}21)$$

$$n^2_o = 1 + E_d \backslash E_o \quad (2\text{-}22)$$

Where: n refractive index, E_d dispersion energy, E_o single oscillator energy of the electronic, n_o static refractive index

Where $E = hv$ is the photon energy. Blotting $(n^2 - 1)^{-1}$ against $(hv)^2$ the investigated film allows to determine the values of the dispersion parameters E_d and E_o. The calculated values of E_d, E_o and the high-frequency dielectric constant.

The energy of dispersion E_d corresponds to the dispersion energy and measures the average strength of interband optical transitions. E_d is the effective oscillator, and E_o is the average strength of interband optical transitions. Ed is related to changes in the structural order of the material, i.e., it is connected to the ionicity, anion valiancy, and coordination number of the material. The single oscillator equation has the benefit of providing an intuitive physical interpretation of the measured values

when fitting experimental data. The average gap, E_o, in particular, provides quantitative information on the material's overall band structure.

This differs from the information obtained from the optical gap E_g (E_o=2E_g), which investigates the material's optical characteristics at the band edges. Localized states near the conduction or valence band "tail states" in particular may have a significant impact on optical absorption and hence reduce the optical gap., whereas if they have a small polarizability, they will result in a small effect on the refractive index: such tail states increase the "Urbach tail", but have little effect on the average gap E_o [67]. The static refractive index, n_o , has been calculated from WDD dispersion parameters, E_o, and, E_d, using the formula (2-22) M_{-3} moments of the optical spectra can be obtained from the relationships [68]. The M_{-1} and M_{-3} moments of the optical spectra can be obtained from the relationships [68]:

$$E^2_o = M_{-1}\backslash M_{-3} \qquad (2\text{-}23)$$

$$E^2_d = M^3_{-1}\backslash M_{-3} \qquad (2\text{-}24)$$

The obtained values are given formula (The M_{-1} and M_{-3} moments changed due to the formation coordination Wimple-DiDomenico.

3.1 Introduction

This chapter emphasizes on the experimental details used in fabrication and investigation of pure Cu_2O thin films with different thicknesses by thermal evaporation method on glass substrate The analysis of structural and morphological aspects by X-ray diffraction (XRD), scanning electron microscope (SEM), and atomic force microscope (AFM), as well as the assessment of grain size, are described as approaches for preparing and testing the structure of thin films. Thin film optical measurements include transmittance (T), absorbance (A), absorption coefficient (α), optical energy gap (E_g), refractive index (n), extinction coefficient (k_o), and dielectric constants (ε_r and ε_i) as well as dispersion parameters for t1 one-layer 25 nm.t_2 one-layer 40 nm, t_3 two-layers 65 nm, and t_4 three-layers 90 nm. Where $t_3 = t_1 + t_2$ and $t_4 = t_1 + t_2 + t_1$. A Fig 3-1 shows a schematic diagram of the experimental study

3.2 Nanomaterial Used:

The copper oxide nanopowder (Cu_2O: 18 nm Super fine 99.86%). The prepared films were deposited as multilayers as in table (3.1)

Table (3.1): The prepared nanolayers of Cu_2O.

Film symbol	No of layers	Thickness (nm)
t_1	1	25
t_2	1	40
t_3	2 = t_1+t_2	65
t_4	3 = t_1+t_2+t_1	90

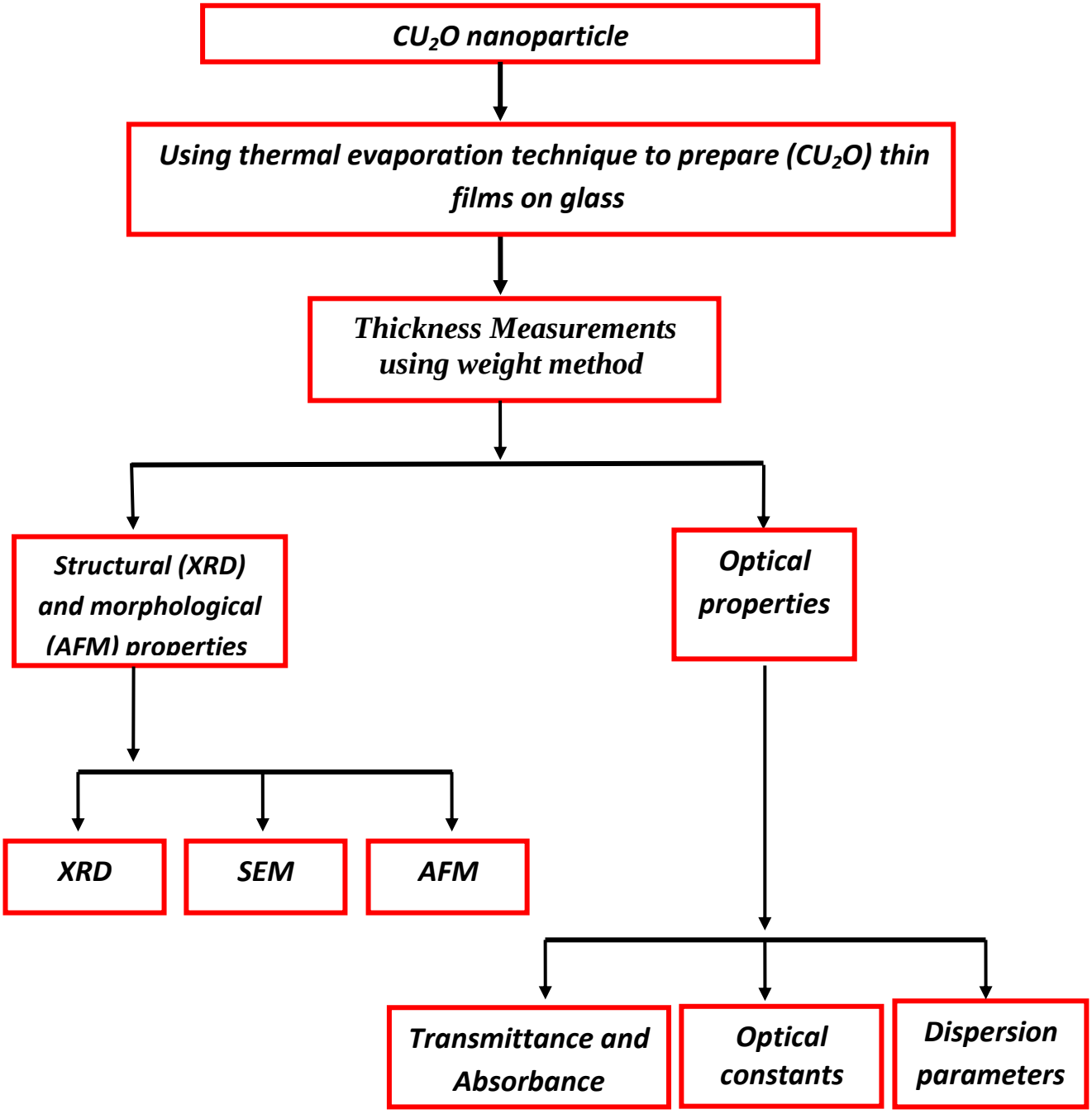

Fig. (3.1) Schematic diagram of experimental work.

3.3 Substrate Preparation

Glass substrate was used for depositing thin films by thermal evaporation, each of (2.54 × 7.62) cm^2 area were used with thickness (0.1-0.12) cm. These glass slides were subjected to the following steps:

1- The substrates were cleaned by alcohol.

2- The substrates were immersed in a clean beaker containing distilled water, and then washed ultrasonically for 10 min.

3- Lastly, the glass substrates were dried by an air-jet and were rubbed with soft paper.

3.4 Evaporation Boat

The most commonly used materials for evaporation boat are metals with a high melting point, such as tungsten (W) (M.P = 3370 ^oC), and molybdenum (Mo) (M.P = 2622 ^oC). In this work, molybdenum boat was used for the deposition of Cu_2O nano-layers, as shown in Fig. (3.2).

Fig. (3.2) Molybdenum Evaporation Boat.

3.5 The Coating Unit

The vacuum unit system is:

1-Edwards Auto 306.

2-Uses Molybdenum filaments to heat evaporates.

3-Ultimate chamber pressure 1×10^{-7} mbar.

4-Typical filament currents are 100-200 A.

5-Maximum deposition thickness that can be achieved is 1.5 μm.

The main constructions of the typical vacuum coating unit are shown in Fig. (3.3).

Fig. (3.3) Thermal evaporation system.

3.6 Thin Film Growth

In the present work, nano-layers of Cu_2O have been obtained by the Cu_2O powder (purity 99.99%). The deposition of Cu_2O films have been performed by electrical resistance heated thermal evaporation process. In this process, the electrical power is passed through the boat to create a vapor which travels in straight line paths to the substrate. In general, there are three steps in any vacuum deposition process, creation of an vapour from the source material, transport of the evaporate from the source to the substrate and condensation of the vapour on to the substrate to form the thin film deposited as in Fig.(3.4). In this work, the evaporation processes have been performed at room temperature (R.T).

The pressure during the evaporation was approximated to 10^{-7} mbar with a rate of deposition 0.5 nm/s The distance between the source and substrate was kept at 15 cm.

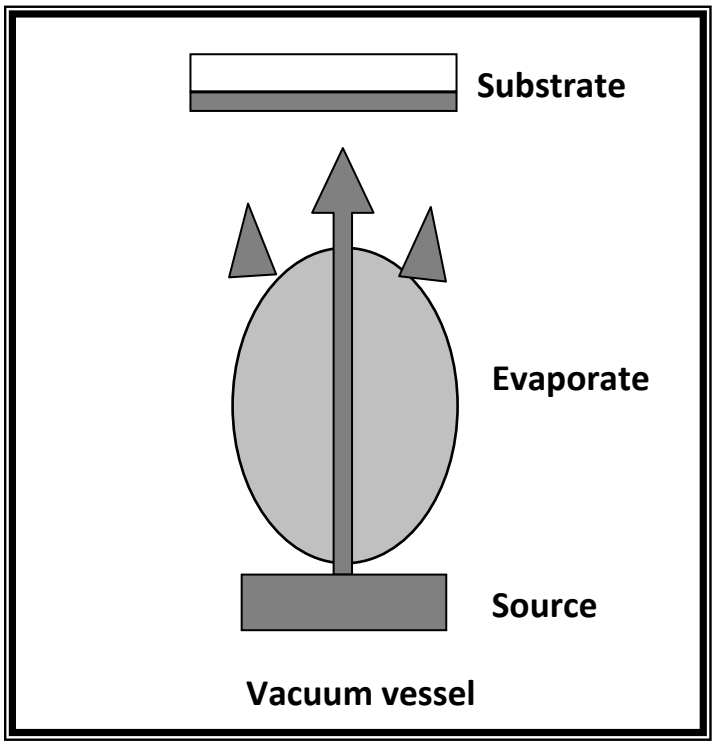

Fig. (3.4) Basic steps deposition processes.

3.7. Measurement of Film Thickness:

One of the most significant thin film parameters is thickness. The thickness of thin film can be measured using a variety of methods. The thickness of the films was assessed using an optical measuring and weight approach in this study.

3.7.1. Optical measurement methods:

Film thickness measurements by optical interferometer method have been obtained. This method is based on interference of the light beam reflection from thin film surface and substrate bottom. He-Ne laser (632 nm) was used, the thicknesses were determined by the difference in optical path lengths of the two reflections, as shown in Fig.(3.5).

Fig. (3.5) Optical thin film measurement.

3.7.2 The weight method

Thickness of the thin films has been calculated allowing to the equation below [1]:

$$t = \frac{m}{2\pi\rho R^2} \quad \text{.....} \quad \text{(3-2)}$$

where:

t: is thickness of the thin films (nm).

m: mass of the material in (g)

ρ: is the density of material (g/cm^3).

R: is the distance between the substrate and the boat (cm).

This method gives an approximate thickness because not all the material is deposited on the substrate but some of the material lost or fleeing on the sides of the heater.

3.8 Structural and Morphological Measurements

3.8.1 X-ray diffraction (XRD)

The main purpose of these measurements is to investigate the type of the structure of the prepared thin films. The entire structure of bulk solids, including lattice constants, identification of unknown materials, orientation of single crystals, orientation of polycrystals, flaws, stresses, and so on, has long been determined using this experimental methodology. SHIMADZU' X-ray diffracts meter (XRD-6000) measures intensity as a function of Bragg's angle. The situation is. CuKα source emitting radiation at a wavelength of 1.5406 Å .

Target: Cu

Current:30 mA.

Voltage:40 kV.

speed of Scanning: 0.25 deg/min

3.8.2 Scanning Electron Microscope (SEM)

In the SEM, a state-of-the-art high resolution LEO 1530 field emission scanning electron microscope with EDX system from OXFORD is available. It is a high performance instrument designed for analytical applications featuring the GEMINI column technology. It is controlled by a 32 bit computer system using Microsoft Windows NT as operating system, The examinations were made at XRD Laboratory - University of Kashan, Iran. as shown in Fig.(3.6)

Fig. (3.6): The system of The SEM

3.8.3.Atomics Forces Microscopies (AFM):

Atomics Forces Microscopies (AFM):enables you to have a look on surfaces on a molecular level. Instead of only pictures real topography data are collected. An atomic force microscope (AFM) is used to determine the size and other parameters of the produced nanoparticles. An AFM's working concept is depicted in Fig (3.7). The AFM is used to examine all of the samples.

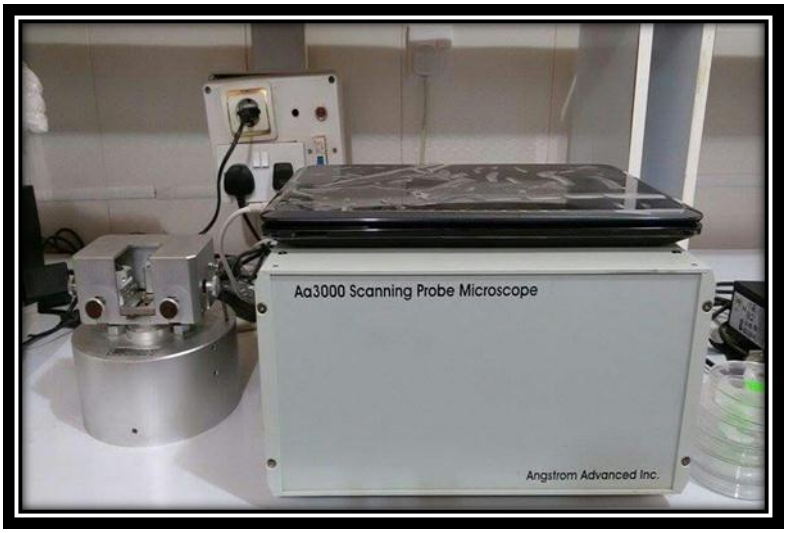

Fig. (3.7) The system of AFM

3. 9 UV-Visible Absorption Spectroscopy

Optical studies of Cu_2O thin films are done with a spectrophotometer (Shimadzu UV-1650 PC) made by Phillips (Japanese firm), as shown in Fig.(3.8), for wavelengths ranging from 200 to 1100 nm. These optical measurements are used to calculate the optical characteristics.

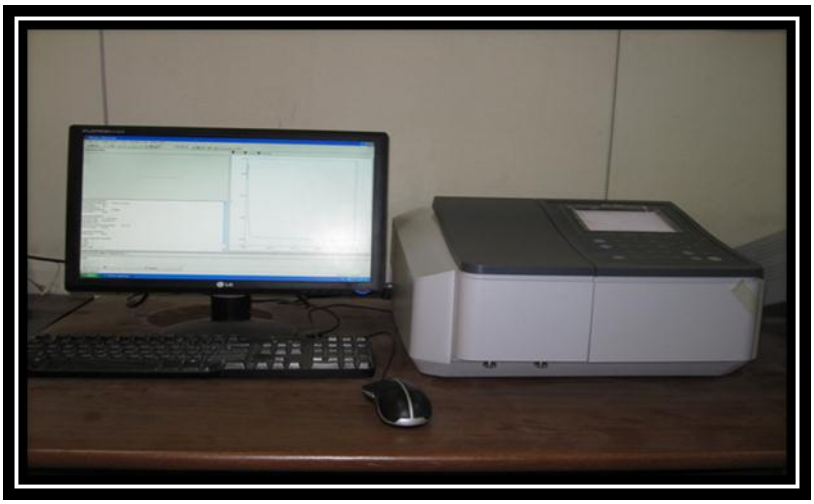

Fig(3.8) shows a photo of a UV-VIS-NIR spectrophotometer.

4.1 Introduction:

This chapter presents the results and discussion of the structural, morphological, and optical properties of Cu_2O nanolayers (the dispersion parameters were also investigated using Wemple-Didominco model) for t_1 one-layer (25 nm), t_2 one-layer (40 nm), t_3 two-layers (65 nm), and t_4 three-layers (90 nm), where $t_3 = t_1 + t_2$ and $t_4 = t_1 + t_2 + t_1$. These are deposited on glass substrates by the thermal evaporation technique.

4.2 Thin Films Test and Results:

After the deposition of the thin films on glass slides was completed, structural and optical tests were performed to determine the effect of the preparation parameters used to prepare them in this study.

4.2.1 Structural and morphological test

The structural characteristics of the thin films produced have been examined using the following technique:

4.2.1.1 X-ray diffraction test:

Test the diagnostic results of X-Ray diffraction (XRD) were shown for Cu_2O films for the four states t_1, t_2, t_3, and t_4, that the crystalline system of the prepared films is of the cubic type. In general, the other crystalline parameters after matching the diffraction peaks that appeared in the X-ray diffraction data with the diffraction peaks of the International Standard Card International Center for Diffraction Data (ICDD) are relevant. The number (01 - 075 - 1531) was with the following specifications shown in Table (4 - 1).

Table (4-1): Crystalline parameters of Cu_2O films (ICDD = 01 - 075 - 1531) prepared on glass slides.

Mineral name	Cuprite	
Compound name	Copper Oxide	
ICSD name	Copper Oxide	
Empirical + Chemical formula	Cu_2O	
Crystal system	Cubic	
Space group	Pn-3m	
Space group number	224	
Unit cell parameters	Lattice constants	a=b=c =4.26A°
	The angle between lattice constants	$\alpha = \beta = \gamma = 90°$

As distinct peaks appeared clearly at the position (2θ° = 29.6, 36.5, 42.4, 61.5, 73.6) of the four samples t_1, t_2 ,t_3 and t_4 the greatest intensity appeared at (2θ° = 36.503), and as shown in Figure (4 – 1A, B, C, and D)

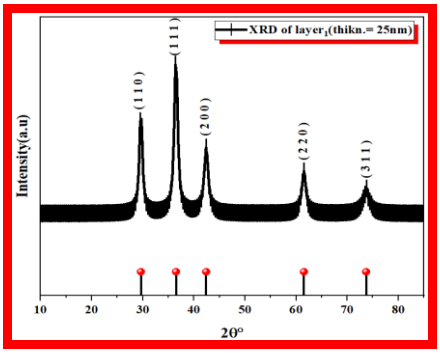

(A)

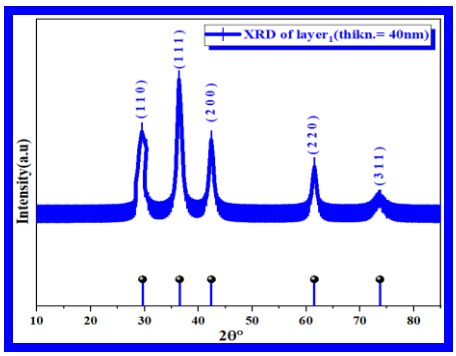

(B)

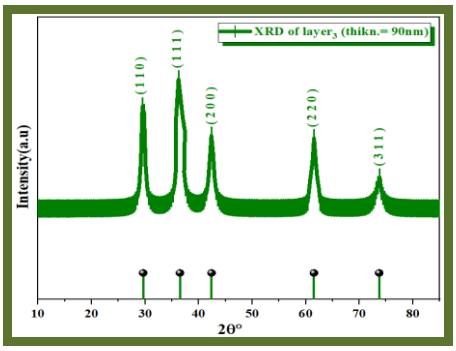

(C)

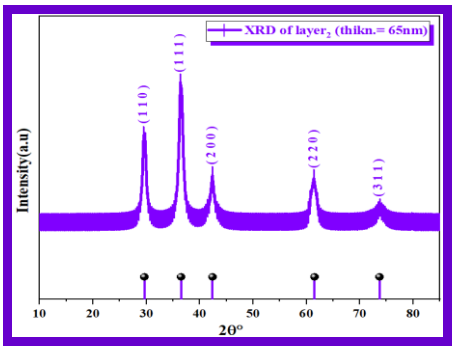

(D)

Fig (4 - 1): XRD pattern of Cu_2O for various layers: A) t_1 one-layer (25 nm), B) t_2 one-layer (40 nm), C) t_3 two-layers (65 nm), and D) t_4 three-layers (90 nm).

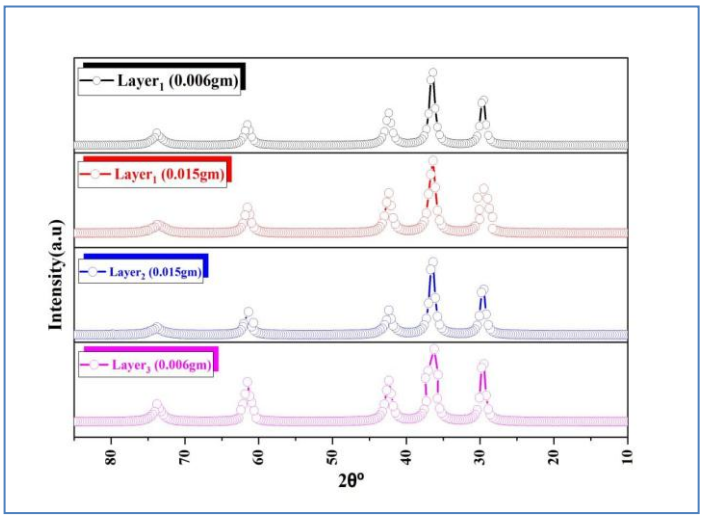

Fig (4 - 2): XRD diffraction pattern of prepared Cu_2O nano-layers.

Crystallite size rate was found based on XRD data using Scherer's Formula, represented by the formula (2-2)

The average Crystallite size, FWHM, and peak position of the prepared thin film grains on the glass slide at the first layer thickness of 25 nm are shows at tables (4 .2)

Tables (4 .2): The average Crystallite size, FWHM, and peak position of the t_1 one- layer (25 nm) sample

peak position (2θ°)	FWHM	D(nm)	Average Crystallite size (nm)
29.449	1.643	4.673	5.220
36.485	1.201	6.277	
42.398	1.198	6.182	
61.520	1.125	6.064	
73.566	2.187	2.906	

The average Crystallite e size, FWHM, and peak position of the prepared thin film grains on the glass slide at the first layer thickness of 40 nm are shown in Table (4 - 3)

Table (4-3): The average Crystallite size, FWHM, and peak position of the t_2 one-layer (40 nm) sample.

peak position (2θ°)	FWHM	D(nm)	Average Crystallite size (nm)
29.631	0.879	8.736	7.099
36.502	0.976	8.139	
42.398	1.182	6.719	
61.520	1.104	7.195	
73.714	1.688	4.704	

The average Crystallite size, FWHM, and peak position of the prepared thin film grains on the glass slide at the third layer thickness of 65 nm are shown in Table (4 - 4):

Table (4-4): The average Crystallite size, FWHM, and peak position of the t_3 two-layers (65 nm) sample.

peak position (2θ°)	FWHM	D(nm)	Average Crystallite size (nm)
29.631	0.880	8.723	6.599
36.502	0.976	8.131	
42.357	1.352	5.873	
61.372	1.277	6.2169	
73.796	1.959	4.053	

The average Crystallite size, FWHM, and peak position of the prepared thin film grains on the glass slide at the fourth layer thickness of 90 nm are shown in Table (4 - 5)

Table (4-5): The average Crystallite size, FWHM, and peak position of the t_4 three-layers (90 nm) sample.

peak position (2θ°)	FWHM	D(nm)	Average Crystallite size (nm)
29.631	0.884	8.684	6.455
36.507	1.437	5.524	
42.398	1.193	6.653	
61.532	1.281	6.198	
73.675	1.523	5.213	

The diffraction pattern and peak positions were the same as those found by D. S. C. Halin and colleagues [69].

4.2.1.2 Scanning Electron Microscopy (SEM):

The scanning electron microscope (SEM) showed the morphology of the Cu_2O films on the glass slide in a high-magnification scan range, the results of the scanning electron microscope were as follows:

The prepared nanofilm of the one-layer with a thickness of 25 nm of scanning electron microscope image represented in fig (4 - 3)

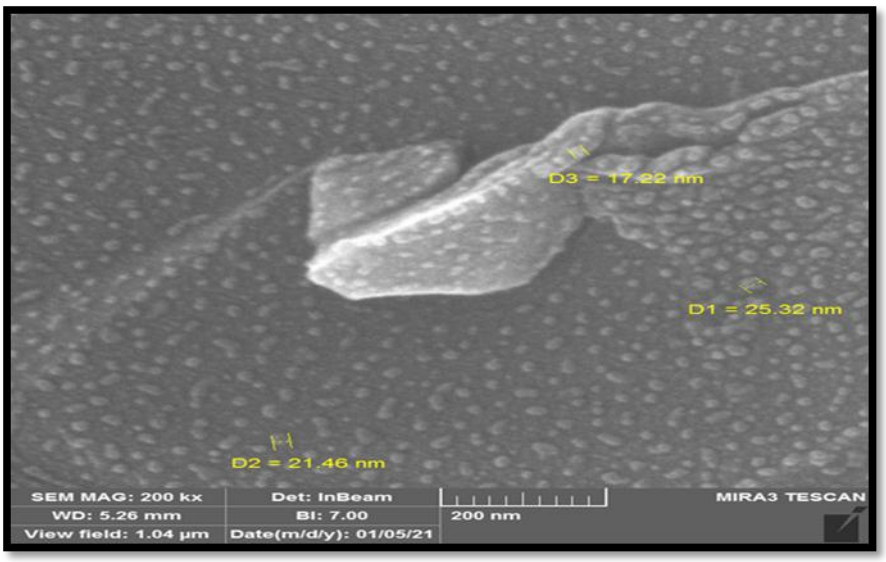

Fig.(4-3): Scanning electron microscope morphology image of t_1 one-layer (25 nm thickness) Cu_2O nanofilm.

It can be seen from the fig a non-compact semi-spherical shape with the emergence of other grains aggregations. The tool Image was used to determine the particle distribution and to calculate the average particle size. The images of the SEM assays showed the particle distribution and grain size value. The diameter of the grains ranged between (8 – 20 nm). The average diameter of the nanoparticles was found to be (11.65 nm), and Fig (4-4) shows these results: A- grains distribution and B- average grain Size.

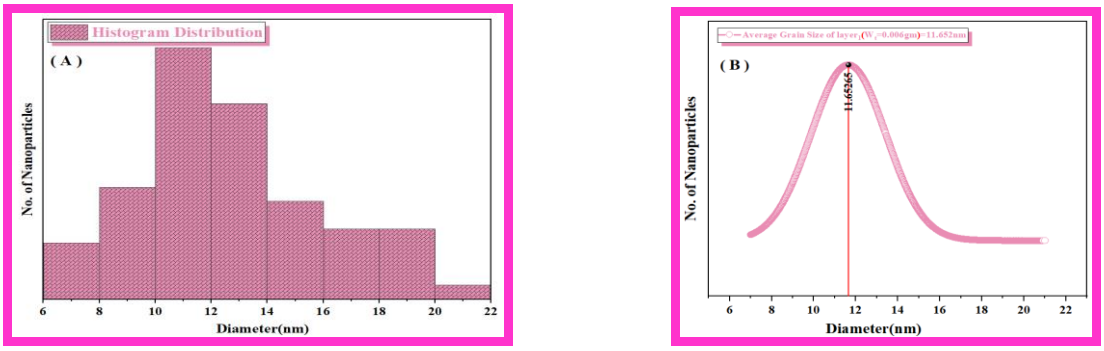

Fig. (4-4): According to the SEM images of the t_1 film of:
a) grains distribution and b) average grain size

The prepared thin film of the first layer with a thickness of 40 nm shows the scanning electron microscope scan picture in fig (4 - 5):

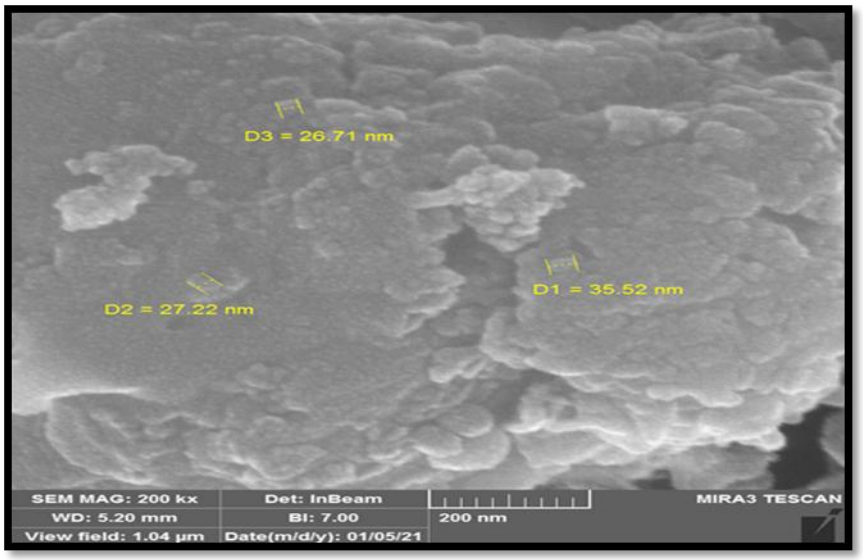

Fig: (4-5) Scanning electron microscope morphology image of t_2 one-layer (40 nm thickness) Cu_2O nanofilm.

It can be seen from the figure a non-compact semi-spherical shape with the emergence of other grains aggregations. The tool Image was used to determine the particle distribution and to calculate the average particle size. The images of the SEM assays showed the particle distribution and grain size value. The diameter of the grains ranged between (8 – 20 nm). The average diameter of the nanoparticles was found to be (9.03 nm), and Fig (4-6) shows these results: A- grains distribution and B- average grain Size.

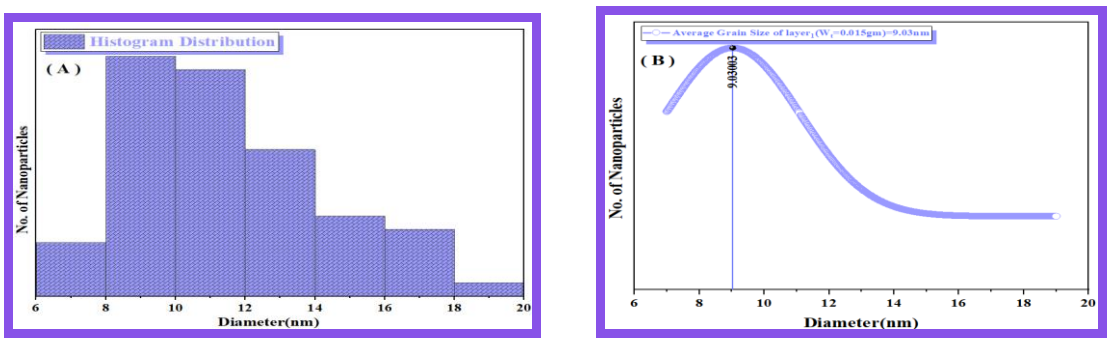

Fig. (4-6): According to the SEM images of the t_2 film of:
a) grains distribution. b) average grain size.

The prepared thin film of the second layer with a thickness of 65 nm shows the scanning electron microscope scan picture in fig (4 - 7):

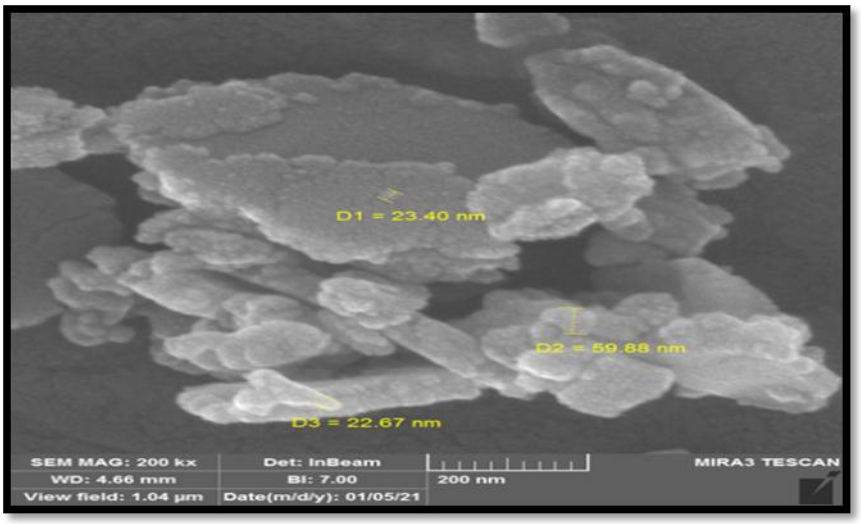

Fig: (4-7) Scanning electron microscope morphology image of t_3 two-layers (65 nm thickness) Cu_2O nanofilm.

It can be seen from the figure a non-compact semi-spherical shape with the emergence of other grains aggregations. The tool Image was used to determine the particle distribution and to calculate the average particle size. The images of the SEM assays showed the particle distribution and grain size value. The diameter of the grains ranged between (8 – 20 nm). The average diameter of the nanoparticles was found to be (11.02 nm), and Figure (4-8) shows these results: A- grains distribution and B- average grain Size.

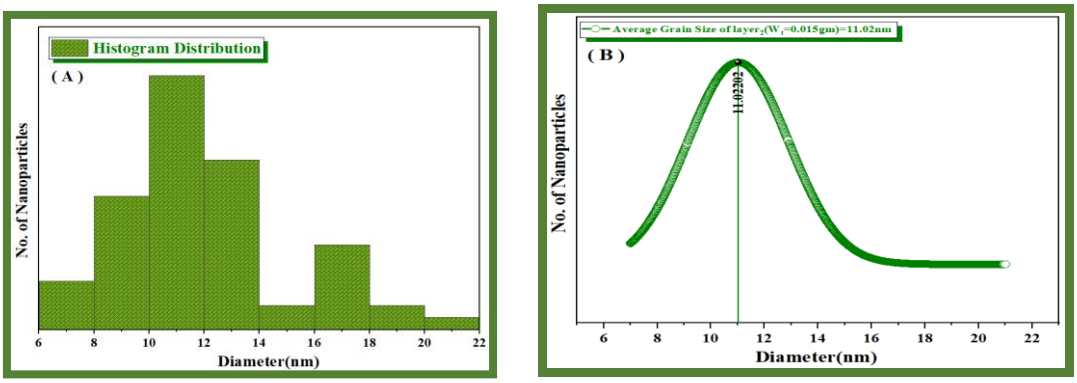

Fig.(4-8): According to the SEM images of the t_3 film of:

b) grains distribution. b) average grain size.

The prepared thin film of the third layer with a thickness of 90nm shows the scanning electron microscope scan image in fig (4 - 9):

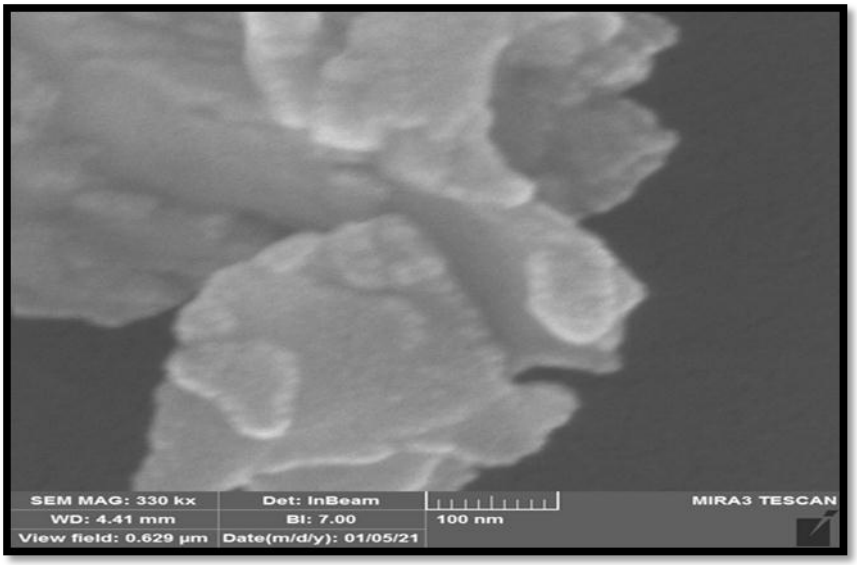

Fig:(4-9) Scanning electron microscope morphology image of t_4 three-layers (90 nm thickness) Cu_2O nano-film.

It can be seen from the fig a non-compact semi-spherical shape with the emergence of other grains aggregations. The tool Image was used to determine the particle distribution and to calculate the average particle size. The images of the SEM assays showed the particle distribution and grain size value. The diameter of the grains ranged between (8 – 20 nm). The average diameter of the nanoparticles was

found to be (10.97 nm), and Figure (4-10) shows these results: A- grains distribution and B- average grain Size.

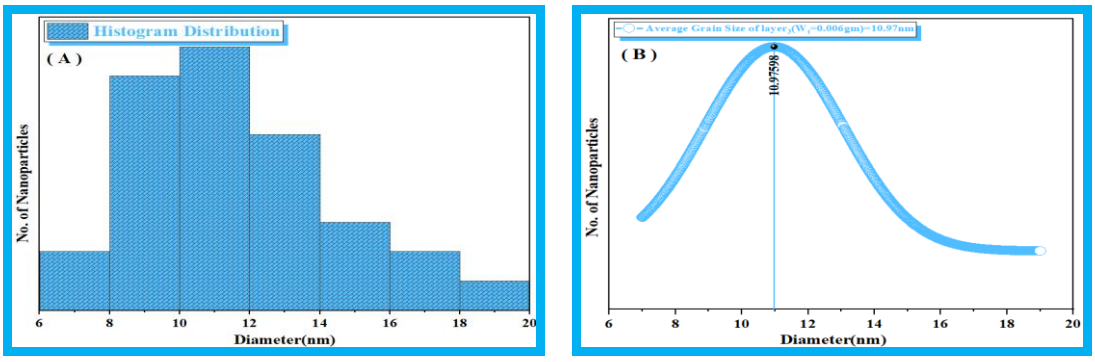

Fig. (4-10): According to the SEM images of the t_4 film of:
a) grains distribution. b) average grain size.

According to the SEM tests, the thicknesses and weights of the layers on which the films were formed and the associated grain sizes for all layers are shown in Table (4 - 6).

Table (4-6): The thicknesses, weights of the layers, and the amounts of granular volumes of the films deposited on these layers.

Layers	Thickness (nm)	Grain size (nm)
1	25	11.65
1	40	9.03
2	65	11.02
3	90	10.97

From the results of the SEM tests, it is clear that the thickness of the layer played an essential role in the nucleation process, which led to the formation of grain clusters that are evident for t_1,t_2,t_3, and t_4 as thin films grains of the first layer appeared homogeneous type Comparison of the growth method of grains for the thin films of the other three layers The above results are roughly in agreement with those of [70-72].

4.2.1.3 Atomic Force Microscope (AFM)

The Atomic Forces Microscopes image of Cu_2O film with different layers and thicknesses of Cu_2O (0.006, 0.015, 0.006) wt.% have been set by thermal evaporation method under the conditions.

The pressure of 1×10^{-7}mbar, degree of deposition 0.5nm.s^{-1}, which are annealed at 573 K temperature for 2 hours and thicknesses of 25 nm (1st layer), 40 nm (1st layer), 65 nm (2nd layer), and 90 nm (3rd layer). As seen in Figs. (4 - 11), the AFM images of the prepared layers reveal uniform granular surface morphology

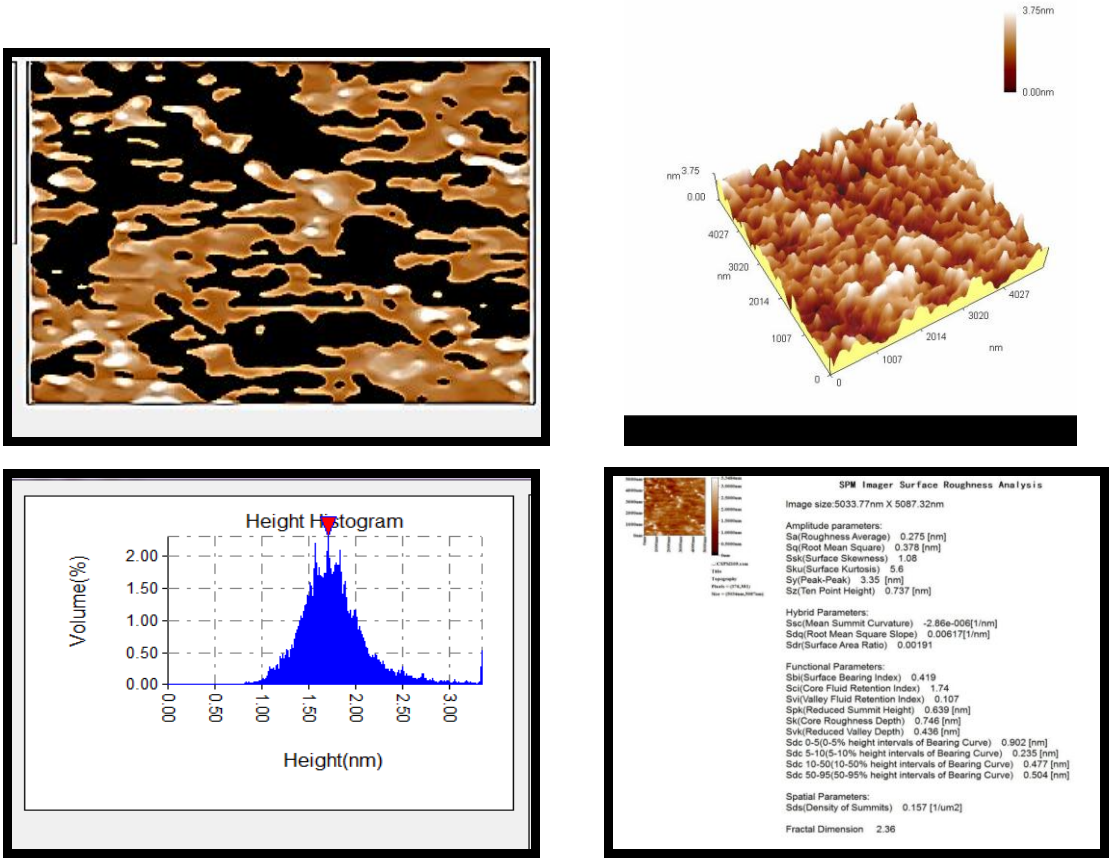

Fig.(4-11): AFM images of Cu_2O nanofilm of t_1 of:
A) Grain distribution, B) 3D, C) Height histogram, and D) 2D image with data report.

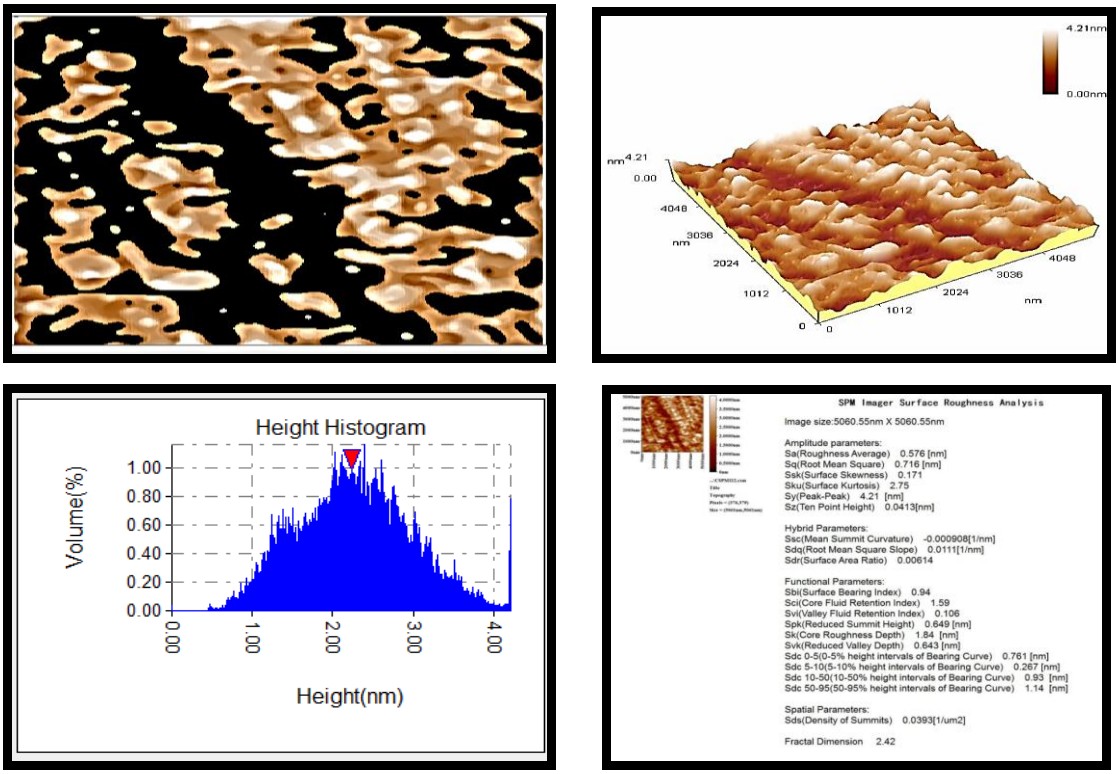

Fig.(4-12): AFM images of Cu_2O nanofilm of t_2 of:

A) Grain distribution, B) 3D, C) Height histogram, and D) 2D image with data report.

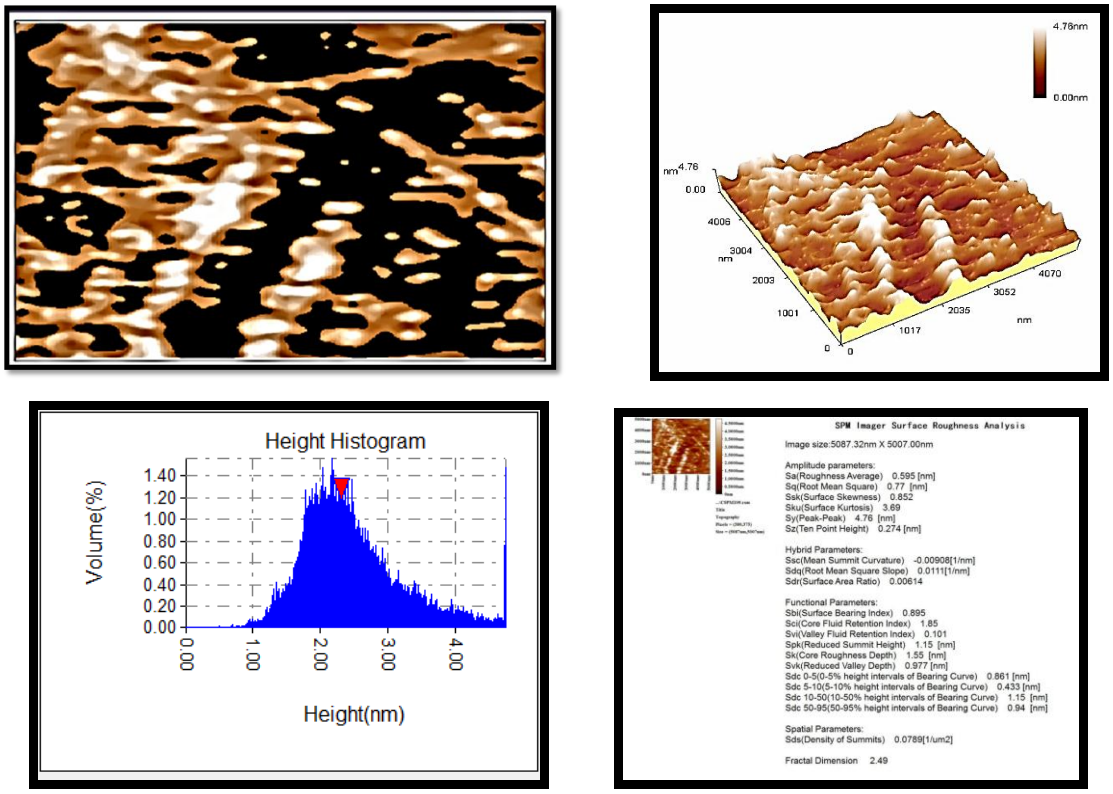

Fig.(4-13): AFM images of Cu_2O nanofilm of t_3 of: A) Grain distribution, B) 3D, C) Height histogram, and D) 2D image with data report

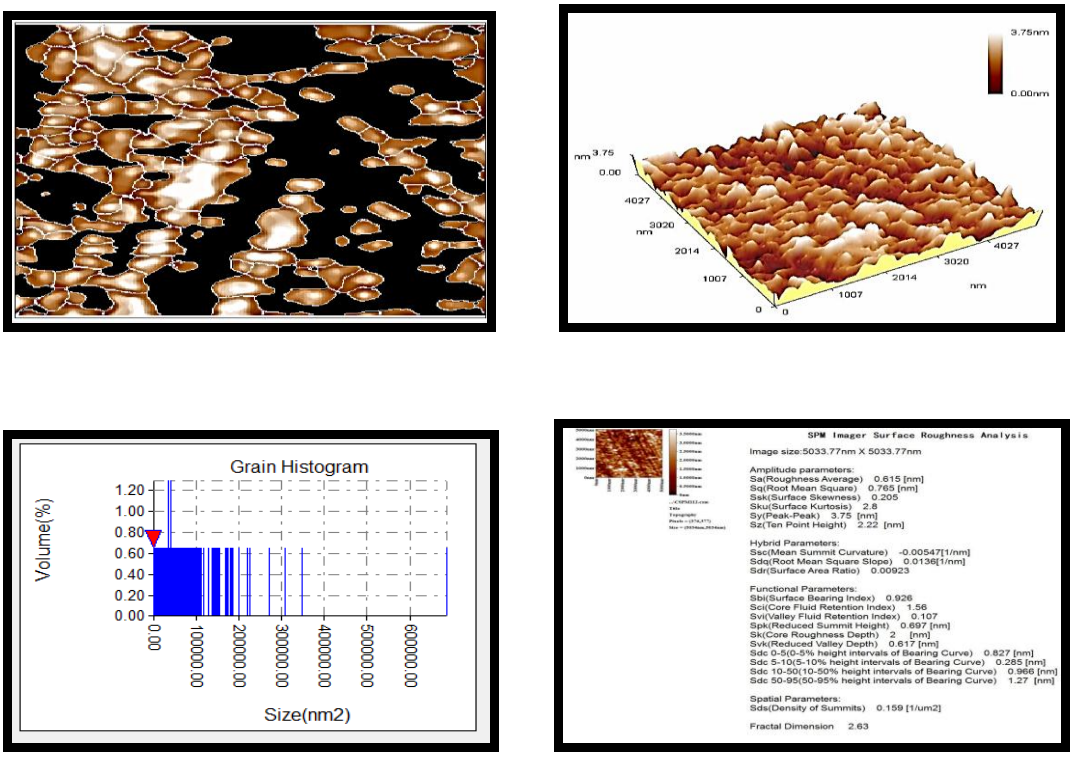

Fig.(4-14): AFM images of Cu_2O nanofilm of t_4 of:

A) Grain distribution, B) 3D, C) Height histogram, and D) 2D image with data report.

From the figures, the high homogeneity of the films appeared from the shallow values of roughness average (ranged from 0.275 to 0.615 nm) and the root means square (ranged from 0.378 to 0.77 nm). The ten-point height refers to the excellent distribution of the material (0.274 to 2.22 nm); the results agree with the finding of the researchers [73-76]. All the results that come from the figures were listed in Table (4 - 7).

Table(4 -7): The AFM parameters of Cu_2O nano-layers.

Number of layers	Thickness (nm)	Roughness average(Sa) (nm)	Root mean square(Sq) (nm)	Ten point height (Sz) (nm)	Average diameter (nm)
1	25	0.275	0.378	0.737	306.8
1	40	0.576	0.716	0.0413	331.3
2	65	0.595	0.770	0.274	322.6
3	90	0.615	0.765	2.220	248.0

4.2.2 Optical Properties:

4.2.2.1 Absorbance (A):

Fig.(4–15) shows the absorbance of (Cu_2O) versus wavelength, the Figure indicates that the absorption rises with Cu_2O layers (thickness), and reduction with wavelength rises [77]. The high absorption of the layers in the UV regions is due to the photon energy being adequate to comply with the atom, the excitation of electrons from a low to a high energy level with absorbing photon energy, and the excitation of electrons from a low to high energy level with absorbing photon energy [78].

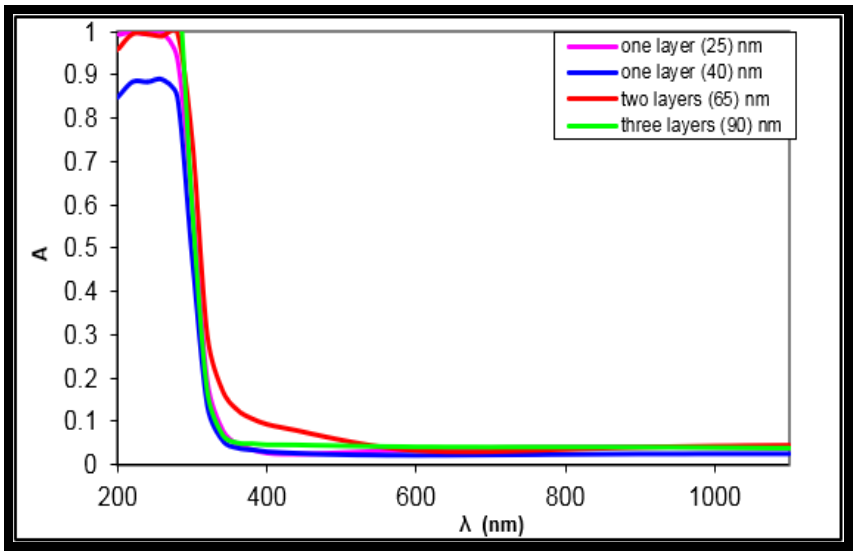

Fig (4-15): The absorbance spectra of Cu_2O nano-layers.

4.2.2.2 Transmittance (T)

The amount of transmittance decreases with increasing thickness, as shown in the graphic relationship between absorbance and wavelength, due to an increase in the number of atoms, which increases the number of photons colliding with incident atoms, resulting in a decrease in the transmittance. As well, the drop in transmittance due to the development of the absorption edge for thin-film became less sharp, which is attributable to the fact that larger crystallite volumes are deposited because since more atoms are found in the material, more states would be required for photons to be absorbed, according to research results[79 -80].

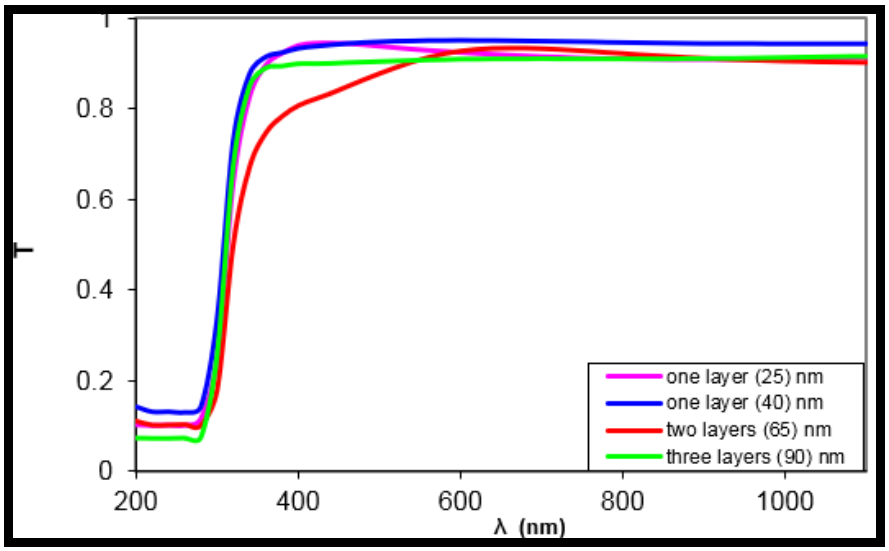

Fig.(4-16): Transmittance spectra of Cu_2O nano-layers.

4.2.2.2 Absorption coefficient (α)

Fig (4-18) displays the optical absorption coefficient as a function of wavelength for (Cu_2O) nano-layers. It was institute that the layers consume a little absorption coefficient at minor photon energy after that growth with rising photon energy depending on the structure of the layers. The study of absorption coefficient spectra might expose the energy gap (E_g) among the valence band and the conduction band due to transitions of direct and indirect for both amorphous and crystalline

materials. The absorption coefficient rises with growth in (Cu_2O) film. The absorption coefficient (α) calculated from the following equation [81]:

$$\alpha = 2.303\frac{A}{t} \dots\dots\dots 4-2$$

where:

A: the absorbance.

t: the thickness of the sample.

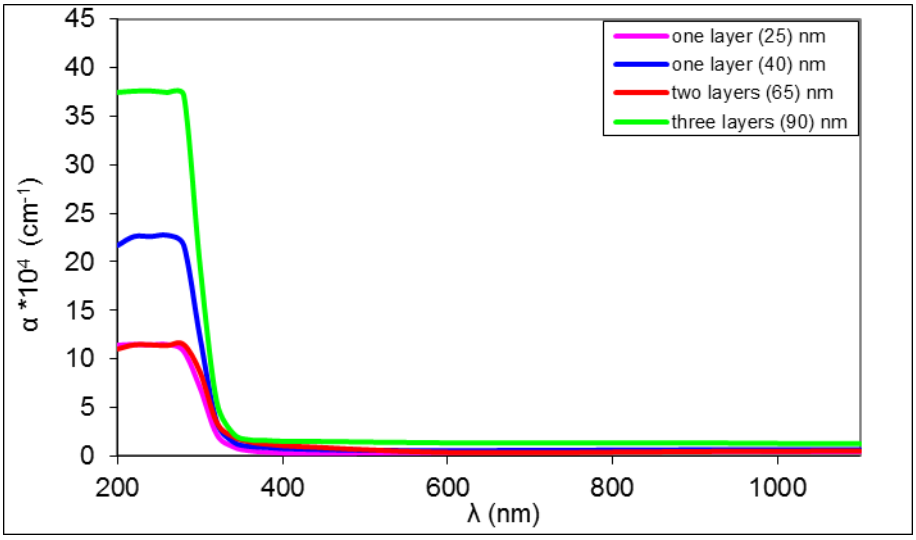

Fig. (4-17): The absorption coefficient of Cu_2O nano-layers.

4.2.2.3 Optical energy gap (E_g):

The variance of direct for permitted transfer as a function of the photon energy of Cu_2O thin film is depicted in Figure (4-18), according to the model of direct transition for amorphous semiconductors planned by Tauc [82].

$$\alpha h\upsilon = B(h\upsilon - E_g)^n \dots\dots\dots 4-3$$

Where: B is a constant related to valance and conduction band properties.

hυ: is photon energy.

E_g: is the optical energy gap difference, and n=1/2 is the permitted direct transfer.

From the direct plots of $(\alpha h\nu)^n$ vs $(h\nu)$ for these samples, as exposed in figure (4- 18), E_g calculated from the extrapolations intercepts to zero with the photon energy axis $(\alpha h\nu)^{1/n} \rightarrow 0$. It is seen that the concentration of (Cu_2O) rising in the system leads to a reduction in E_g. This might be recognized as structural disorder growth of the thin film with growing (Cu_2O) layers.

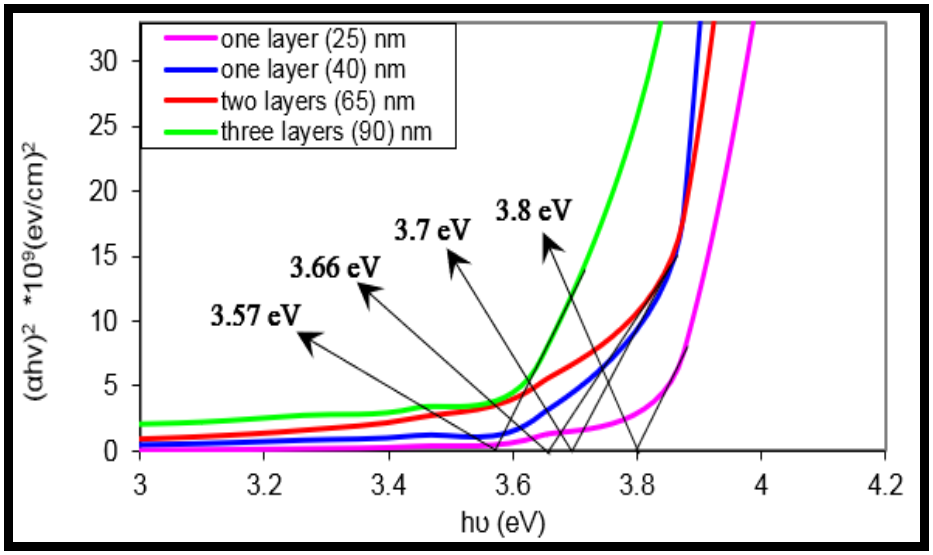

Fig. (4-18): The relationship between $(\alpha h\nu)^{1/2}$ and photon energy for Cu_2O nano-layers.

From figure (4 – 19), the energy gap reduced from 3.8 eV to 3.57 eV when the film thickness increased from 25 nm to 90 nm.

4.2.2.4 Extinction Coefficient (K) and Refractive Index (n):

Fig (4-20) and (4-21) show the difference of the extinction coefficient (k) and refractive index (n) for Cu_2O thin films as a function of wavelength. The extinction coefficient was determined by used equation (4 -4) [83-84]:

$$k = \frac{\alpha\lambda}{4\pi} \dots\dots\dots 4-4$$

Where:

λ: is the wavelength.

α: is the absorption coefficient.

While the refractive index of the film calculated by the following equation [85]:

$$n = \frac{R+1}{R-1} + \sqrt{\frac{4R}{(1-R)^2} - K^2} \dots\dots\dots 4-5$$

Where:

R: is the reflectance.

k: is the extinction coefficient, the k values rise with growing (Cu_2O) layers.

This growth shows that the electromagnetic radiation is transient faster in the temporary photon energy with low levels through the material. This is the increment of photons dispersion and optical absorption in the prepared layers [85]. In contrast, the refractive index n rising with an increment of Cu_2O layers and reduced with an increment of wavelength. This performance may be observed when the layers of Cu_2O get thicker or as a variation in the absorption coefficient, which leads to a spectrum variation in the charge polarization location.

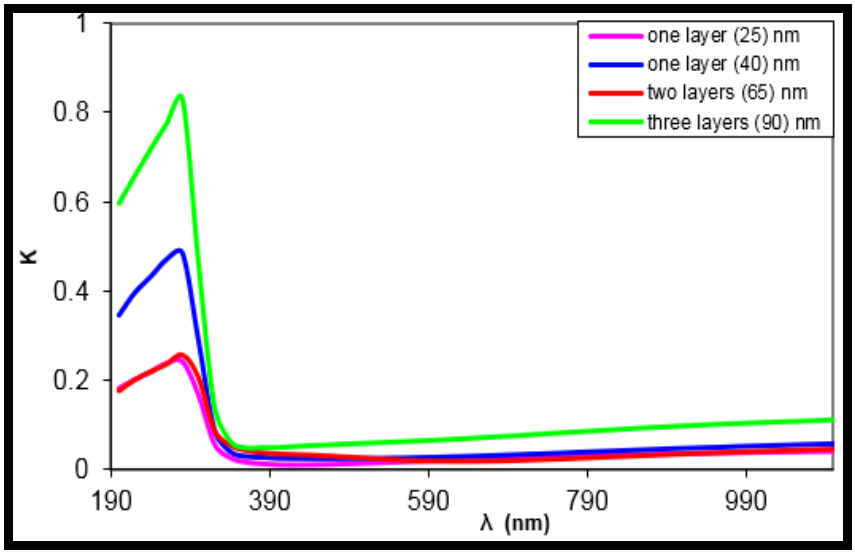

Fig. (4-19): Variation of the extinction coefficient as a function of wavelength for Cu_2O nanofilms.

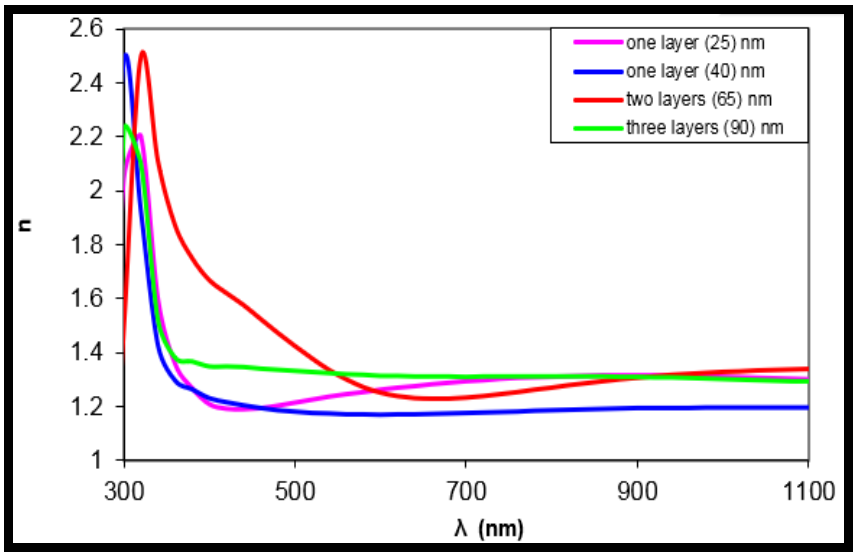

Fig. (4-20): Variation of refractive index as a function of wavelength for Cu_2O nanofilms.

Equations can be used to measure the actual and imaginary parts of the dielectric constant (ε_1 and ε_2). [86]:

$$\varepsilon = \varepsilon_1 - i\varepsilon_2 \dots\dots\dots 4-6$$

$$\varepsilon_1 = n^2 - k^2 \dots\dots\dots 4-7$$

$$\varepsilon_2 = 2nk \dots\dots\dots 4-8$$

The actual and imaginary portions of the dielectric constant are plotted against the incident wavelength as in Fig (4 – 22) and (4 – 23).

With the growth of Cu_2O layers, the real and imaginary portions of the dielectric constant were improved because of the extinction coefficient and refractive index amassed [87].

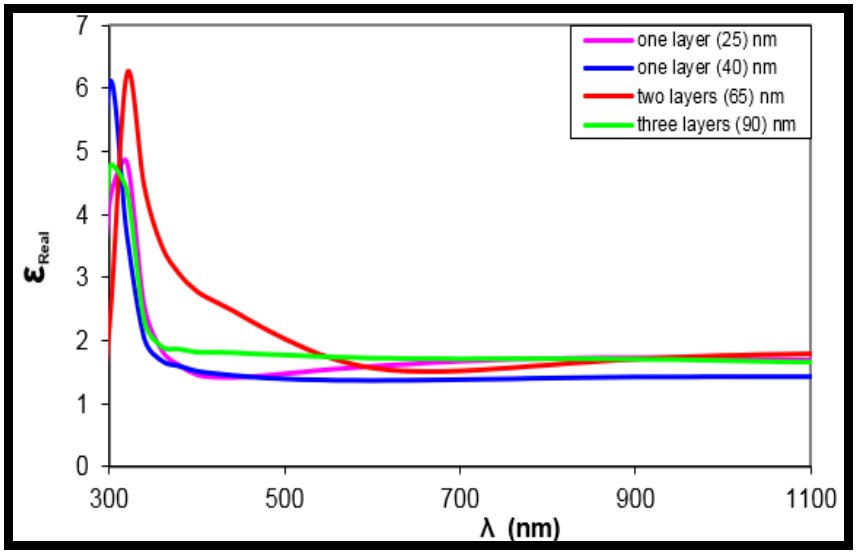

Fig. (4-21): The variation of the real part of dielectric constant as a function of wavelength for Cu_2O nanofilms.

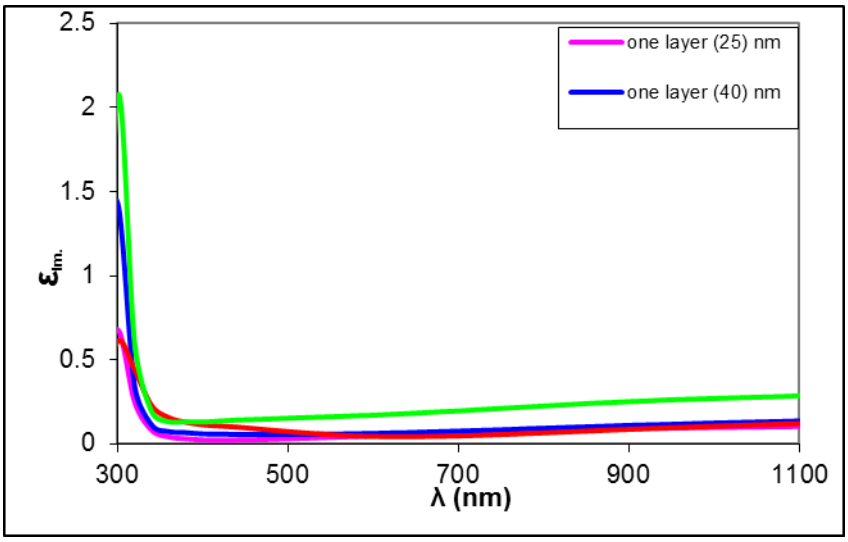

Fig (4-22): The variation of the imaginary part of dielectric constant as a function of wavelength for Cu_2O nanofilms.

4.2.2.5 Dispersion parameters:

Dispersion parameters were studied and diagnosed using Wemple DiDomenico model. The quantities of Were M_{-1},M_{-3} calculated from the equations (2-22) and (2-23) And by drawing the graphic relationship

between $(n^2-1)^{-1}$ **and** $(h\upsilon)^2$ for the four layers: layer$_1$(25 nm), layer$_1$(40 nm), layer$_2$(65 nm), layer$_3$(90 nm), As shown in Figures (4-23), (4-24), (4-25) and (4-26), it is clear from these figures that the values of E_d, E_o decrease with the increase in the thickness of the layer, as shown in Table (4 – 8):

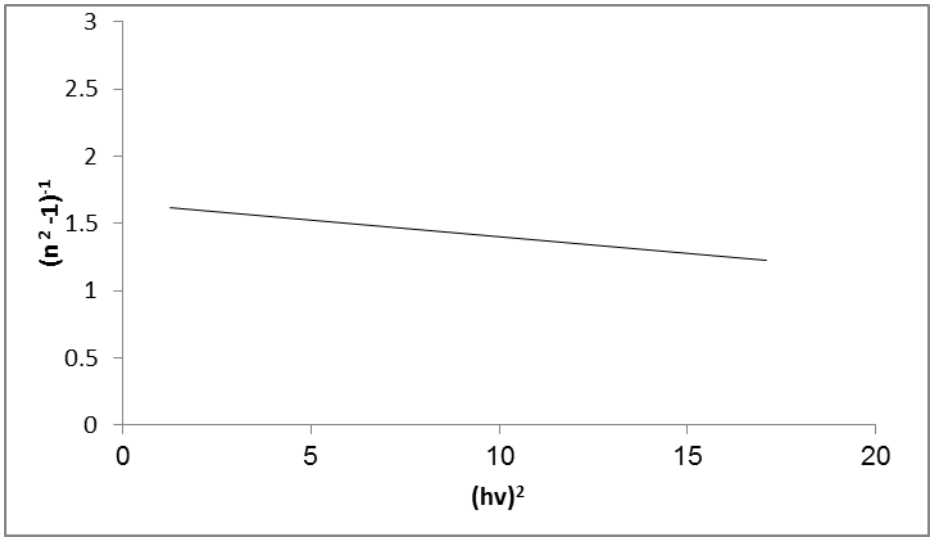

Fig (4-23): The relation of the $(n^2-1)^{-1}$ versus $(h\upsilon)^2$ of Cu_2O nanofilms of t_1.

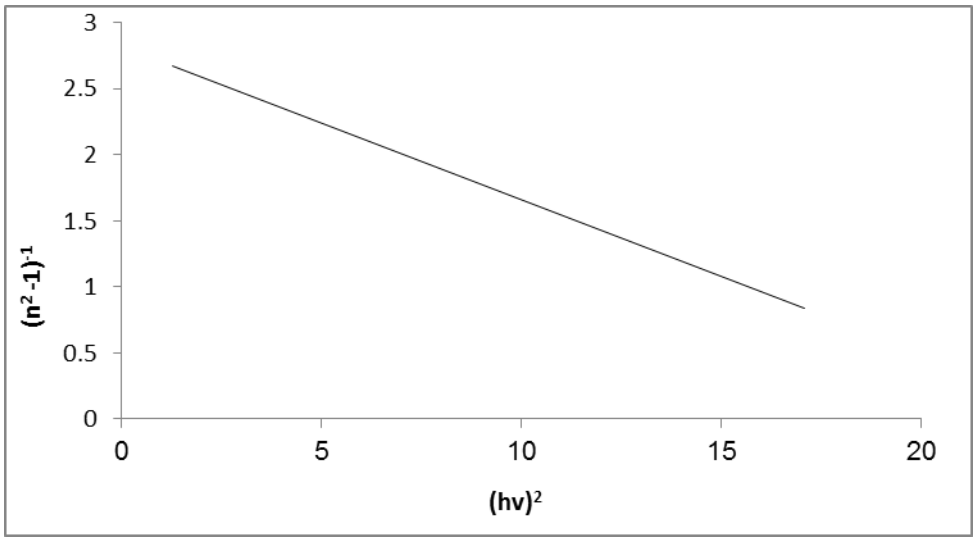

Fig (4-24): The relation of the $(n^2-1)^{-1}$ versus $(h\upsilon)^2$ of Cu_2O nanofilms of t_2.

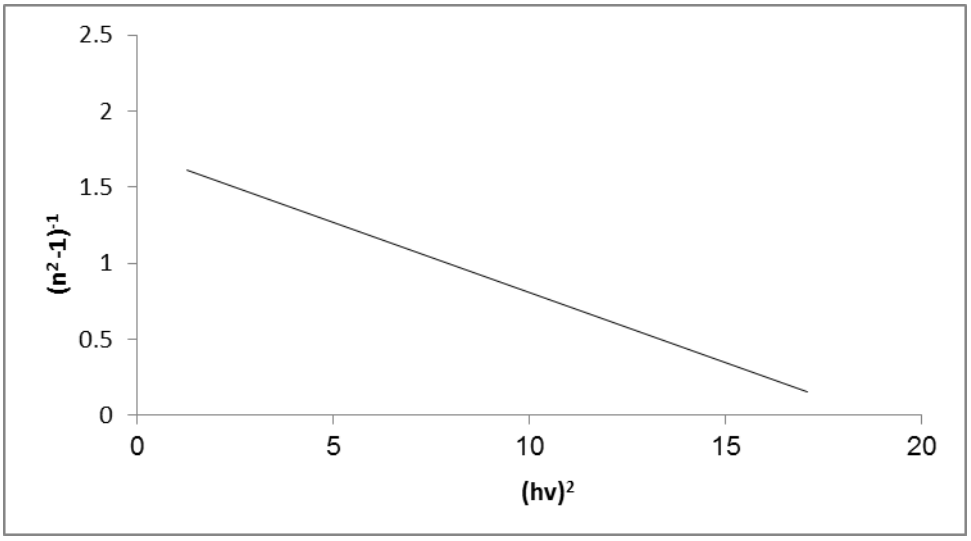

Fig (4-25): The relation of the $(n^2-1)^{-1}$ versus $(h\upsilon)^2$ of Cu_2O nanofilms of t_3.

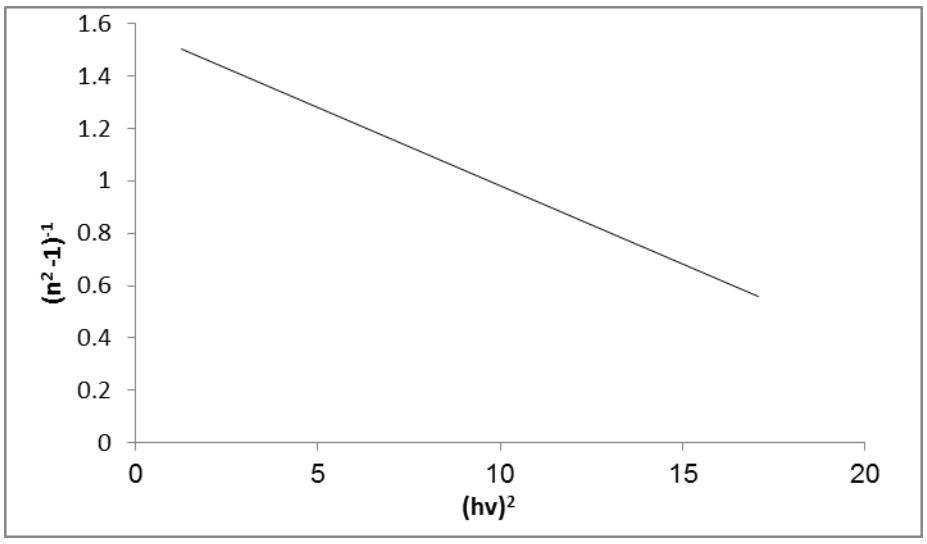

Fig (4-26): The relation of the $(n^2-1)^{-1}$ versus $(h\upsilon)^2$ of Cu_2O nanofilms of t_4.

Table (4-8): Urbach energy and optical parameters of Cu_2O thin films

Thickness	E_d (eV)	E_o(eV)	E_g (eV)	ε_∞	n_o	M_{-1}	M_{-3}
25 nm	5.61	8.9	4.45	2.26	1.50	0.26	0.003
40 nm	1.90	5.2	3.60	1.86	1.36	0.24	0.520
65 nm	2.70	6.6	3.30	1.75	1.32	0.34	0.016
90 nm	7.80	6.3	3.15	2.23	1.49	0.44	0.011

Conclusions

1- The Cu_2O nanalayers were successfully prepared using thermal evaporation technique for (t_1 ,t_2, t_3, t_4)

2- Obtained Cu_2O nanalayers with cubic and crystal systems resulted from X-ray diffraction test. Obtain grain sizes within the nanoscale (5 -8 nm) for grains prepared on the four thicknesses using the Debye-Scherer equation refer to quantization effect.

3- The particle size within the range (9 -12 nm) resulted from SEM images refer to quantization effect, make the layers have a high surface area and a high ability to interact, which candidate it in solar cell application.

4- A uniform granular surface shows morphology of the atomic force microscope (AFM) images of thin films. The average roughness and the root mean square (RMS) are increased with the increasing of Cu_2O ratio and thickness, where RMS is increased from 0.378 nm for thickness 25 nm and from 0.716 nm for thickness 40nm and from 0.770 nm thickness 65 nm and from 0.765 nm for thickness

5- The absorbance of (Cu_2O) versus wavelength, indicates that the absorption rises with Cu_2O layers (thickness), and reduction with wavelength rises because of free electron number rising that absorbed of the light incident amount and the transmittance decreases with increasing of thickness, due to an increase in the number of atoms, which increases the number of photons colliding with incident atoms, resulting in a decrease in the transmittance, furthermore the optical energy gap for four layers were respectively decreases from (3.57-3.8 eV). the high energy gap refers to the quantization effect

6- Dispersion parameters were studied and diagnosed using Wemple DiDomenico model the dispersion energy ,oscillating energy,energy gap and momentum were obtained

Future Projects

1. Using other types of deposition substrate such as quartz, silicon, or porous silicon to deposited Cu_2O thin films.
2. Using other deposition methods (chemical or physical) with the same parameters of preparation and deposition of Cu_2O films approved in this study.

3- Using other parameters for deposition of Cu_2O thin films, such as changing the thickness of the layers or weight.

References

[1] K. L. Chopra, "Thin film devices application", Plenum press, New York, (1983).

[2] L. Eckortova, "Physics of thin films", Plenum press, (1977).

[3] W. Knoll, and R. C. Advincula, " Functional Polymer Films", Vol. 2, (2013).

[4] K. L. Chopra, "Thin Film Phenomena", McGraw Hill, New York, (1969).

[5] J. M. Pearce, N. Podraza, R. W. Collins, M. M. Al-Jassim, K. M. Jones, J. Deng, C. R. Wronski, "Optimization of open circuit voltage in amorphous silicon solar cells with mixed-phase (amorphous + nanocrystalline) p-type contacts of low nanocrystalline content", Journal of Applied Physics, Vol. 101, No. 11, pp. 114301, (2007).

[6] M. A. Green, "Crystalline and thin-film silicon solar cells: state of the art and future potential", Solar Energy, Vol. 74, No. 3, pp. 181-192, (2003).

[7] M. Cernea, "Methods for preparation of $BaTiO_3$ thin films", Journal of Opotoelectronics and Advanced Materials, Vol. 6, No. 4, pp. 1349 (2004).

[8] VA. Myamlin, YV. Pleskov, "Electrochemistry of Semiconductors", Plenum Press, New York, NY, USA, (1967).

[9] W. G. Adams and R. E. Day, "The action of light on selenium", Proceedings of the Royal Society A, Vol. 25, pp. 113 (1877).

[10] M. Causa, R. Dovesi, C. Pisani, C. Roetti, Surface Science, Vol. 175, pp. 551, (1986).

[11 H. Gerischer, H. Tributsch, H. Electrochemische "Untersuchungen zur spectraleu sensibilisierung von ZnO-Einkristallen" ,Vol. 72, pp. 437-445, (1968).

[12] K. Hauffe, HJ. Danzmann, H. Pusch, J. Range, H. Volz, "New Experiments on the sensitization of zinc oxide by means of the electrochemical cell technique", Vol. 117, pp. 993-999, (1970).

[13] J. Furer, "Growth of Single-Wall Carbon Nanotubes by Chemical Vapor Deposition for Electrical Devices", Ph. D Thesis, Basel University, (2006).

[14] N. Habashi, "What is nanotechnology - a brief introduction in the form of simplified lessons", King Fahad National Library, Riyadh, Saudi Arabia, Vol. 1, (2009).

[15] RB. Gupta, UB. Kompella, "Fundamentals of drug nanoparticles-drugs and the pharmaceutical sciences. A series of textbooks and monographs. Nano particles technology for drug delivery", Taylor and Francis Group, New York, USA, Vol. 159 , pp. 1-199, (2006).

[16] SK. Sahoo, S. Parveen, "The present and future of nanotechnology in human health care Nanomedicine", Vol. 3, pp. 20-31, (2007).

[17] D. Liu, W. Wu, Y. Qiu, S. Yang, S. Xiao, Q. Q. Wang, L. Ding, and J. Wang, "Surface functionalization of ZnO nanotetrapods with photoactive and electro-active organic monolayers", Journal of Langmuir, Vol. 24, pp. 5052, (2008).

[18] S. Sze and K. Kwok, "Physics of semiconductor devices", 3rd ed, John Wiley and Sons, New York, (2006).

[19] N. N. Greenwood, A. Earnshaw, Chemistry of the Elements, 2nd ed., Butterworth-Heinemann, Oxford, UK, 1997.

[20] H. Wayne Richardson "Copper Compounds in Ullmann's Encyclopedia of Industrial Chemistry 2002, Wiley-VCH, Weinheim.

[21] C. C. Tseng, J. H. Hsieh, S. J. Liu, and W. Wu, "Effects of Ag contents and deposition temperatures on the electrical and optical behaviors of Ag-doped Cu_2O thin films," Thin Solid Films, vol. 518, no. 5, pp. 1407–1410, 2009.

[22] H. Xu, W. Wang, and W. Zhu, "Shape evolution and size-controllable synthesis of Cu_2O octahedra and their morphology-dependent photocatalytic properties," J. Phys. Chem. B, vol. 110, no. 28, pp. 13829–13834, 2006

[23] D. Nicholls, Complexes and First-Row Transition Elements, Macmillan Press, London, 1973..

[24] L. O. Grondahl, Unidirectional current carrying device,Patent, 1927

[25] Hanke, L.; Fröhlich, D.; Ivanov, A. L.;Littlewood, P. B.; Stolz, H.(1999-11-22). "LA Phonoritons in Cu_2O". Physical Review Letters.83 (21):4365–4368. doi:10.1103/PhysRevLett.83.4365

[26] L. Brillouin: Wave Propagation and Group Velocity, Academic Press, New York City, 1960 ISBN 9781483276014

[27] J. Brandt, D. Fröhlich, C.Sandfort, M.Bayer, H. Stolz, and N. Naka,Ultranarrow absorption and twophonon excitation spectroscopy of Cu2O paraexcitons in a high magnetic field, Phys. Rev. Lett. 99, 217403 (2007).doi:10.1103/PhysRevLett. 99.217403

[28]. J. P. Wolfe and A. Mysyrowicz:Excitonic Matter,Scientific American 250 (1984), No. 3, 98

[29] . Hopfield, J. J. (1958). "Theory of the Contribution of Excitons to the Complex Dielectric Constant of Crystals". Physical Review.112 (5):1555–1567. doi:10.1103/PhysRev.112.1555 .ISSN 0031-899X .

[30] Jeong, S., Song, S. H., Nagaich, K., Campbell, S. A., & Aydil, E. S. (2011). An analysis of temperature dependent current–voltage

characteristics of Cu_2O–ZnO heterojunction solar cells. *Thin Solid Films*, *519*(19), 6613-6619.

[31] Kidowaki, H., Oku, T., Akiyama, T., Suzuki, A., Jeyadevan, B., & Cuya, J. (2012). Fabrication and characterization of CuO-based solar cells. *Journal of Materials Science Research*, *1*(1), 138.

[32] Gershon, T., Musselman, K. P., Marin, A., Friend, R. H., & MacManus-Driscoll, J. L. (2012). Thin-film ZnO/Cu_2O solar cells incorporating an organic buffer layer. *Solar energy materials and solar cells*, *96*, 148-154.

[33] Paracchino, A., Brauer, J. C., Moser, J. E., Thimsen, E., & Graetzel, M. (2012). Synthesis and characterization of high-photoactivity electrodeposited Cu2O solar absorber by photoelectrochemistry and ultrafast spectroscopy. *The Journal of Physical Chemistry C*, *116*(13), 7341-7350.

[34] Noda, S., Shima, H., & Akinaga, H. (2013, April). Cu_2O/ZnO heterojunction solar cells fabricated by magnetron-sputter deposition method films using sintered ceramics targets. In *Journal of Physics: Conference Series* (Vol. 433, No. 1, p. 012027). IOP Publishing.

[35] Yu, L., Xiong, L., & Yu, Y. (2015). Cu2O homojunction solar cells: F-doped N-type thin film and highly improved efficiency. *The Journal of Physical Chemistry C*, *119*(40), 22803-22811.

[36] Sboui, M., Bouattour, S., Gruttadauria, M., Liotta, L. F., La Parola, V., & Boufi, S. (2016). Hybrid paper–TiO_2 coupled with a Cu_2O heterojunction: an efficient photocatalyst under sun-light irradiation. *RSC advances*, *6*(90), 86918-86929

[37] Zang, Z. (2018). Efficiency enhancement of ZnO/Cu_2O solar cells with well oriented and micrometer grain sized Cu2O films. *Applied Physics Letters*, *112*(4), 042106.

[38] Sekar, P. (2020). Metal oxide nanostructure for sensor applications. *International Journal of Progressive Research in Science and Engineering*, *1*(3), 154-166.

[39] Tuama, A., Abass, K. H., Hamzah, M., Mezan, S., & Agam, M. B. (2020). Morphological and optical properties of cuprous oxide nano films for solar cell application. *Test Eng. Manag*, *83*(13090), 13090-13099

[40] Kara, R., Lahmar, H., Mentar, L., Siab, R., Kadirgan, F., & Azizi, A. (2020). Electrochemical growth and characterization of Cu_2O: Na/ZnO heterojunctions for solar cells applications. *Journal of Alloys and Compounds*, *817*, 152748.

[41] Kumar, N., Parui, S. S., Limbu, S., Mahato, D. K., Tiwari, N., & Chauhan, R. N. (2021). Structural and optical properties of sol–gel derived CuO and Cu_2O nanoparticles. *Materials Today: Proceedings*, *41*, 237-241.

[42] Alsultany, F. H., Alhasan, S. F. H., & Salim, E. T. (2021). Seed Layer-Assisted Chemical Bath Deposition of Cu_2O Nanoparticles On ITO-Coated Glass Substrates With Tunable Morphology, Crystallinity, and Optical Properties. *Journal of Inorganic and Organometallic Polymers and Materials*, 1-11.

[43] J. L. Vossen and W. Kern, "Thin film processes II", Boston academic press, (1991).

[44] J. M. Lafferty, "Vacuum : from art to exact science", Phys. today, Vol.34, No.11, pp.211–231, (1981).

[45] R. W. Bery, P. M. Hall and M. T. Harris, "Thin film technology", Van Nostrand Reinhold Company, (1968).

[46] D. M . Mattox, "Foundations of vacuum coating technology", William Andrew publishing/Noyes, (2003).

[47] C. Giacovazzo, "Fundamentals of x-ray crystallography", Oxford University Press, (1998).

[48] S. M. Sze, "Physics of semiconductor devices", 2nd Ed., John Wiley and Sons, (1981).

[49] J. Solgom, "Fundamentals of the physics of solids: Structure and Dynamics", Springer Berlin Heidelberg, Vol.1, New York, (2007).

[50] C. Gumus, O. M. Ozkendir, H. Kavak, and Y. Ufuktepe, "Structural and optical properties of zinc oxide thin films prepared by spray pyrolysis method", J. Optoelectronics and advanced materials, Vol.8, pp.299-303, (2006).

[51] A. A. Ansari, M. Alhoshan, M. S. Alsalhi, and A. S. Aldwayyan, "Chapter 2: Nanostructured metal oxides based enzymatic electrochemical biosensors." Biosensors, InTech, (2010).

[52] C. E. Lyman, D. E. Newbury, J. I. Goldstein, D. B. Williams, A. D. Romig, J. T.Armstrong, P. Echlin, C. E. Fiori, D. C. Joy, E. Lifshin and K. Peters, "Scanning Electron Microscopy, X-Ray Microanalysis and Analytical Electron Microscopy: A Laboratory Workbook." Plenum Press. New York, (1990).

[53] R. Wiesendanger, "Scanning probe microscopy and spectroscopy." Cambridge University Press, (1994).

[54] L. R. Johnson, "Characterization of piezoelectric ZnO thin films and the fabrication of piezoelectric micro-cantilevers." Iowa State University, (2005).

[55] Y. N. Al-Jamal, "Solid state physics", Al-Mosel University, 2nd ed., Arabic Version, (2000).

[56] R. A. Smith, "Semiconductors", Cambridge press, 2nd ed., (1987).

[57] B. G. Stereeman, "Solid state electronic devices", 2nd ed, Practice hall, Inc. Engle wood cliffs, N. J., (1980).

[58] A. G. Nilens, "Deep imparity in semiconductors", Wiley -Interscience publication, (1973).

[59] J. I. Pankove, "Optical process in semiconductors", Dover Publishing, Inc., New York, (1971).

[60] C. Kittel, "Introduction to solid state physics", 5th ed., Willy, New York, (1981).

[61] A. N. Donald, "Semiconductor physics and devices", Irwin, USA, (1992).

[62] J. Jaffe and A. Zunger, "Electronic structure of the ternary pnictide semiconductors $ZnSiP_2$, $ZnGeP_2$, $ZnSnP_2$, $ZnSiAs_2$, and $MgSiP_2$", Phys. Rev., Vol.28, No.49, pp.1882-1905, (1984).

[63] D. Bonnell, B. Huey and D. Carroll, "In-situ measurement of electric fields at individual grain boundaries in TiO_2", Solid state ionics, Vol.75, pp.35-42, (1995).

[64] J. Marien, T. Wagner, G. Duscher, A. Koch and M. Rühle, "Ag, Pt, Pd, Nb doping (110) TiO_2 (Rutile), growth, structure, and chemical composition of the interface", surface sci., Vol.446, p.219, (2000).

[65] M. Nnabuchi, "Optical and solid state characterization of optimized manganese sulphide thin films and their possible applications in solar

energy", The pacific J. of Sci. and technology, Vol.7, No.1, pp.69-76, (2006).

[66] N. Amin and T. Isaka, "Effect of substrate temperatures on CdSe:Sn thin films", J. Appl. Phys., Vol.38, (2000).

[67] Solomen I , Schmidt M P , Senemaud C , Khodja M D , *Physical Review* , **1988**, B38, 13263.

[68] Yakuphanoglua F, Cukurovalib A and Yilmazb I , *Physica* , **2004**, B351, 53.

[69] D. S. C. Halin, I. A. Talib, A. R. Daud, and M. A. A. Hamid, "Cu2O thin film for photoelectrochemical solar cell (PESC) of ITO/Cu2O/PVC-LiClO4/graphite," *AIP Conf. Proc.*, vol. 1835, no. January, 2017, doi: 10.1063/1.4981845.

[70] C. A. N. Fernando, P. H. C. De Silva, S. K. Wethasinha, I. M. Dharmadasa, T. Delsol, and M. C. Simmonds, "Investigation of n-type Cu2O layers prepared by a low cost chemical method for use in photo-voltaic thin film solar cells," *Renew. Energy*, vol. 26, no. 4, pp. 521–529, 2002, doi: 10.1016/S0960-1481(01)00157-4.

[71] P. N. Hishimone, H. Nagai, M. Morita, T. Sakamoto, and M. Sato, "Highly-conductive and well-adhered Cu thin film fabricated on quartz glass by heat treatment of a precursor film obtained via spray-coating of an aqueous solution involving Cu(II) complexes," *Coatings*, vol. 8, no. 10, 2018, doi: 10.3390/COATINGS8100352.

[72] A. A. Hssi *et al.*, "Growth and characterization of Cu_2O for solar cells applications," *AIP Conf. Proc.*, vol. 2056, pp. 2–8, 2018, doi: 10.1063/1.5084979.

[73] Abass, K.H., Adil, A., Mohammed, M.K., Fabrication and enhancement of SnS:Ag/Si solar cell via. thermal evaporation

technique, Journal of Engineering and Applied Sciences, 13(4), pp. 919-925, 2018.

[74] Sharba, K.S., Alkelaby, A.S., Sakhil, M.D., Abass, K.H., Habubi, N.F., Chiad, S.S., Enhancement of urbach energy and dispersion parameters of polyvinyl alcohol with Kaolin additive, NeuroQuantology, 18(3), pp. 66-73, 2020.

[75] Ehssan Salah Hassan, KameranYasseenQader, EsraaHassnHadi, Sami Salman Chiad, Nadir FadhilHabubi, and Khalid HaneenAbass, Sensitivity of Nanostructured Mn-Doped Cobalt Oxide Films for Gas Sensor Application, Nano Biomed. Eng., Vol. 12, No. 3, pp. 205-213, 2020.

[76] Alaa Nihad Tuama, KhalidHaneenAbass, MohdArifAgam, Fabrication and Characterization of Cu_2O:Ag/Si Solar Cell Via Thermal Evaporation Technique, International Journal of Nanoelectronics and Materials Vol. 13, No. 3, p.p 601-614, 2020.

[77] D. Hegazy, M. Eid and M.Madani,Effect of Ni Nanoparticles on Thermal, Optical and Electrical Behavior of Irradiated PVA/AAc Films, Arab Journal of Nuclear Science and Applications, Vol. 47, No. 1, pp. 41-52, (2014).

[78] I.A.Pal, and M.S. Gaur, Optical Properties of Solution Growth PVDF-ZnO Nanocomposites Thin Films, Journal of Polymer Research, Vol. 20, No. 43, pp. 1-8, (2013).

[79] Abass, K.H., Latif, D.M.A., The urbach energy and dispersion parameters dependence of substrate temperature of CdO thin films prepared by chemical spray pyrolysis, International Journal of ChemTech Research, 9(9), pp. 332-338, 2016.

[80] M. F. Alias, R. M. Aljarrah, H. Kh. Al-Lamy, and K. A. Adem, Investigation the effect of thickness on the structural and optical properties of nanoZnO films prepared by dc magnetron sputtering,

International J. of application or innovation in engineering & management, Vol.2, No.7, pp.198-203, (2013).

[81] Adnan KURT, 2010, Influence of $AlCl_3$ on the optical properties of new film, Turk J Chem.

[82] C. Mwolfe, N. Holouyak and G. B. Stillman, (1989). Physical properties of Semiconductor, prentice Hall, New York.

[83] O. G. Abdullah and S. R. Saeed, 2013, Effect of NaI doping on same physical characteristic of (PVA)0.9-(KHSO4)0.1 composite films, Chemistry and Materials Research, Vol.3, No. 11, (2014).

[84] Al Asadi, S.M., Hamood, F.J., Abass, K.H., Mohammed, S.K., Hassan, I.M., Latif, D.M.A., The effect of MgO nanoparticles on structure and optical properties of PVA-PAAm blend, Research Journal of Pharmacy and Technology, 12(6), pp. 2768-2771, 2019.

[85] Z. A. Al-Ramadani, J. A. Salman and H.A. Hmud, optical and Morphological Properties of (PVA-PVP-Ag) Nanocomposites, International Journal of Science and Research, Vol. 5, (2016).

[86] W. A. Al-Dulaimi,Study the Optical Properties of Methyl Blue Doped Polyvinyl Alcohol International Journal of Physics and Application, Vol. 8, No. 1, PP. 25-31, (2016).

[87] O.G. Abdullah, Influence of Barium Salt on Optical Behavior of PVA Based Solid Polymer Electrolytes , Eoropian Scientific Journal, Vol. 10, No. 33, (2014).

الخلاصة

في هذا العمل، حضرت الأغشية النانوية من أوكسيد النحاس النقي (Cu_2O) بسماك مختلفة t_1 و t_2 و t_3 و t_4 وبتقنية التبخير الحراري تحت ضغط ١ × ١٠$^{-٧}$ ملي بار، معدل الترسيب ٠.٥ نانومتر / ثانية على ارضيات زجاجية في درجة حرارة الغرفة.

أظهرت نتائج حيود الأشعة السينية (XRD) لأغشية Cu_2O المحضرة على شرائح زجاجية أن النظام البلوري للأغشية المحضرة من النوع المكعب. درست تضاريس السطح باستخدام مجهر القوة الذرية (AFM). حيث أثبتت القياسات أن الأغشية المحضرة بهذه الطريقة لها سطح متجانس. يزداد متوسط الخشونة والجذر المتوسط التربيعي ومتوسط قطر الحبيبات بزيادة السمك. أظهر الفحص المجهري الإلكتروني (SEM) قطر الحبيبات. تراوح قطر الحبيبات ما بين ٨-٢٠ نانومتر. كان متوسط قطر الجسيمات النانوية ١١.٦٥ نانومتر، ٩.٠٣ نانومتر١٠.٩٧ نانومتر ١١.٠٢ نانومتر للاغشية t_1 و t_2 و t_3 و t_4 على التوالي.

أظهرت نتائج الخواص البصرية أن امتصاص اغشية Cu_2O يزداد مع السمك، بينما تقل النفاذية. ايضا الثوابت البصرية مثل معامل الامتصاص و معامل الانكسار و معامل الخمود و ثوابت العزل الحقيقي والخيالي ومعاملات التفريق.

جمهورية العراق
وزارة التعليم العالي والبحث العلمي
جامعة بابل
كلية التربية للعلوم الصرفة
قسم الفيزياء

طبقات نانوية من Cu_2O محضرة بتقنية التبخير الحراري لتطبيقات الالكترونيات الضوئية

رسالة مقدمة
الى مجلس كلية التربية للعلوم الصرفة جامعة بابل كجزء من متطلبات
الحصول على درجة الماجستير في التربية/ الفيزياء

من قبل
آيات عباس عبيد
بكالوريوس تربية في الفيزياء ٢٠١٧
(جامعة بابل ٢٠١٧م)
بإشراف
أ.د. خالد حنين عباس

٢٠٢١ م ١٤٤٣ هـ